HELSINKI UNIVERSITY OF TECHNOLOGY
Department of Engineering
Physics and Mathematics

Jukka Katainen

# Determination of the adsorption structure of benzene on Co(0001)



Master's thesis submitted in partial fulfilment of the requirements for the degree of Master of Science in Technology.

Espoo, February 25, 2002

| | |
|---|---|
| Supervisor | Professor Pekka Hautojärvi |
| Instructor | Docent Jouko Lahtinen |

HELSINKI UNIVERSITY OF TECHNOLOGY
DEPARTMENT OF ENGINEERING
PHYSICS AND MATHEMATICS

ABSTRACT OF MASTER'S THESIS

| | |
|---|---|
| **Author:** | Jukka Katainen |
| **Department:** | Department of Engineering Physics and Mathematics |
| **Major:** | Applied Physics |
| **Minor:** | Microelectronics |
| **Title:** | Determination of the adsorption structure of benzene on Co(0001) |
| **Title in Finnish:** | Bentseenin adsorptiorakenteen selvittäminen Co(0001) pinnalla |
| **Chair:** | Tfy-3 Applied Physics |
| **Supervisor:** | Professor Pekka Hautojärvi |
| **Instructor:** | Docent Jouko Lahtinen |

**Abstract:** We have studied the adsorption of benzene on Co(0001) with low energy electron diffraction (LEED). Benzene was adsorbed on the surface and the intensity of three integral and seven fractional order beams were recorded as a function of incident electron energy. Measured IV-curves were used in detailed structure analysis. The analysis was done with tensor–LEED.

Benzene was found to adsorb molecularly on Co(0001) at room temperature and below. Two different adsorption structures were observed on the surface: A $c(2\sqrt{3} \times 4)rect$ superstructure was observed at room temperature and with low coverages below room temperature. A $p(\sqrt{7} \times \sqrt{7})R19.1°$ superstructure was observed below room temperature with higher coverages. The ideal coverages of the structures are $\theta = 0.125$ (former) and $\theta = 0.143$ (latter).

From the saturated $p(\sqrt{7} \times \sqrt{7})R19.1°$ structure, LEED–IV-curves were recorded resulting in a total of ten beams with a total energy span of 1640 eV. Seven of them were used in the IV-analysis.

As a result of the IV-analysis, benzene molecules were found to adsorb on a hcp hollow site with parallel C–C bonds aligned in $[1\bar{1}00]$ direction. The length of the C–C bonds equaled the gas phase value. Analysis also indicated a slight buckling of the benzene ring.

Adsorption of benzene also caused changes on the substrate: The first and the second substrate layers buckled and the distances between the topmost atomic layers relaxed.

| | | | |
|---|---|---|---|
| **Keywords:** | LEED, cobalt, benzene, aromatics, adsorption | | |
| **Pages:** | 58+19 | **Date:** | February 25, 2002 |
| **Approved:** | | **Library code:** | |

TEKNILLINEN KORKEAKOULU
TEKNILLISEN FYSIIKAN JA
MATEMATIIKAN OSASTO

DIPLOMITYÖN TIIVISTELMÄ

| | |
|---|---|
| **Tekijä:** | Jukka Katainen |
| **Osasto:** | Teknillisen fysiikan ja matematiikan osasto |
| **Pääaine:** | Sovellettu fysiikka |
| **Sivuaine:** | Mikroelektroniikka |
| **Työn nimi:** | Bentseenin adsorptiorakenteen selvittäminen Co(0001) pinnalla |
| **Title in English:** | Determination of the adsorption structure of benzene on Co(0001) |
| **Professuuri:** | Tfy-3 Sovellettu fysiikka |
| **Valvoja:** | Professori Pekka Hautojärvi |
| **Ohjaaja:** | Dosentti Jouko Lahtinen |

**Tiivistelmä:** Olemme tutkineet bentseenin adsorptiota Co(0001) pinnalla. Päätutkimusmenetelmänä käyttettiin matalaenergisten elektronien diffraktiota (LEED). Bentseenin peitossa olevalta Co(0001) pinnalta mitattiin kolmen kokonaisluku- ja seitsemän murtolukudiffraktiosuihkun intensiteetit tulevien elektronien energian funktiona. Näin saatuja intensiteettikäyriä käytettiin yksityiskohtaisen pintarakenteen selvittämiseen. Analyysi tehtiin Tensor–LEED ohjelmistolla.

Bentseenin todettiin adsorboituvan molekyyleinä Co(0001) pinnalle huoneenlämpötilassa ja sen alapuolella. Bentseenin peitossa olevalla pinnalla havaittiin kaksi eri adsorptiorakennetta: $c(2\sqrt{3}\times4)rect$ -rakenne havaittiin huoneenlämpötilassa kaikilla peitoilla sekä matalammassa lämpötilassa pienillä peitoilla. $p(\sqrt{7}\times\sqrt{7})R19.1°$ -rakenne puolestaan havaittiin alle huoneen lämpötilassa suuremmilla peitoilla. Rakenteiden ideaaliset peitot ovat $\theta = 0.125$ edelliselle ja $\theta = 0.143$ jälkimmäiselle.

Saturoituneesta $p(\sqrt{7}\times\sqrt{7})R19.1°$ -rakenteesta mitattiin yhteensä kymmenen diffraktiosuihkun intensiteetti–jännitekäyrät vastaten 1640 eV:n energia-aluetta. IV-analyysiin näistä käytettiin seitsemää.

Analyysin perusteella voimme todeta bentseenimolekyylien olevan adsorboituneina hcp paikoille, yhdensuuntaiset C–C-sidokset $[1\bar{1}00]$ suuntaisina. Bentseenimolekyylin C–C-sidokset pysyivät saman pituisina kuin bentseenin olleessa kaasumaisena. Analyysi osoitti myös bentseenirenkaan lievää vääntymistä pinnalla.

Bentseenin adsorptio aiheutti myös muutoksia koboltin pinnalla: Ensimmäinen ja toinen atomikerros kumpuilivat ja ylimpien kerrosten kerrosten väliset etäisyydet relaksoituivat.

| | | | |
|---|---|---|---|
| **Avainsanat:** | LEED, koboltti, bentseeni, adsorptio | | |
| **Sivumäärä:** | 58+19 | **Päivämäärä:** | 25.2.2002 |
| **Hyväksytty:** | | **Työn sijaintipaikka:** | |

# Preface

In 1997 I started at Helsinki University of Technology. Four and a half years of studies: books, exercises and exams; Four and a half years of hilarious student life: parties, lazy afternoons and evening beers with friends. I know I am going to miss all that.

Now it is time to move on. However, before that, I would like to express my gratitude to people who have had an influence on my studies and particularly on this work, done in the Laboratory of Physics between June 2001 and February 2002.

I would like to thank Professor Pekka Hautojärvi for the opportunity to do this work and Docent Jouko Lahtinen for guidance and advice he has given me during the work. M.Sc. Karin Habermehl-Ćwirzeń also deserves compliments for working with me; thank you. I am also obliged to Docent Matti Lindroos and M.Sc. Katariina Pussi in the Laboratory of Computational Physics at Tampere University of Technology. M.Sc. Jani Sainio and M.Sc. Lauri Salminen have had time to listen to me whenever I have had something in my mind. Thanks for the time wasted on those conversations.

Since studying is not only hard work, I would like to thank those people who have, at least every now and then, managed to keep me away from the studies. Those moments have been joyful. Also, I would like to thank Driving school's president Veikko Sompa since he has tried to delay my graduation to the last; apparently with unsatisfactory results.

Finally, I would like to thank my parents for the support they have offered me during my studies.

Espoo, February 25, 2002

Jukka Katainen

# Contents

# Chapter 1

# Introduction

Aromatic compounds are important raw materials for chemical industry. Aromatics are used for example in production of pigments, explosives, detergents and plastics. In order to develop processes in which aromatics are used, the physics behind the chemical reactions is of fundamental importance. However, studying the physical interaction behind some chemical reaction may be difficult or even impossible, since the reacting species and the process itself are usually very complex.

Benzene, $C_6H_6$, is the simplest aromatic molecule and it can be used as a model for more complex aromatic compounds. Investigating simplified benzene systems may provide useful information on more complex systems and improve the understanding of chemical processes where aromatics are involved. Especially, the determination of the adsorption geometry of benzene on transition metal surfaces is of major importance in order to understand the elementary steps of the dissociation and catalyzed reactions of aromatics.

Benzene has interested surface scientists for years and the adsorption of benzene on several transition metal surfaces has been studied. The studies have been made e.g. on Ru(0001) [1, 2, 3, 4], Ni(111) [5, 6, 7, 8, 9], Rh(111) [10, 11, 12] and Pt(111) [13, 14]. Characteristic for the adsorption of benzene on these surfaces is the molecular adsorption at high coverages and the flat orientation of the molecule on the surface. Some distortion of the molecule is also detected.

Adsorption studies require a special environment. In atmospheric pressures studies of the well defined surface are not possible since the ambient molecules impinging the surface cause significant contamination of the sample. In order to create well defined and reproducible surfaces for adsorption studies UHV (Ultra High Vacuum) conditions have to be used. In UHV range, when the pressure is under $10^{-9}$ Torr, the contamination of the surface is lowered to a level where the surface can be cleaned and maintained clean for several hours needed for the measurements. In addition many techniques used in surface studies, e.g. electron spectroscopies, require high vacuum conditions.

Low Energy Electron Diffraction (LEED) is a very useful method for investigating the adsorbed overlayers. It is highly surface sensitive and it provides information on the overlayer geometry. In addition to LEED, other methods like XPS (X-ray Photoelectron Spectroscopy) and TDS (Thermal Desorption Spectroscopy) have to be used, since LEED provides information only on the adsorption structure and not, for example, degradation of adsorbed species. With the simultaneous use of several methods, desorption process and interactions between the adsorbate and the substrate can be studied in detail.

Detailed analysis, however, can be done only with simplified systems, since the real catalysts are too complex. Simple and well defined surfaces are used in surface studies instead of real catalysts. Usually the surface studies use some low index single crystal surface, since the preparing of the surface is easy and reproduction of the well defined conditions on the surface is possible.

In this work adsorption of benzene on Co(0001) single crystal surface has been studied. Fundamental research has been done earlier [15] and the aim of this work is to continue the studies and obtain information on the adsorption geometry of benzene on Co(0001) by LEED. To be exact, the goal of the work is to determine the adsorption phases of benzene and to analyze the adsorption geometry in detail. In order to do this a set of LEED–IV-curves was measured and analyzed.

This work was a collaboration between the Laboratory of Physics at Helsinki University of Technology and the Laboratory of Computational Physics at Tampere University of Technology.

# Chapter 2

# Theoretical aspects of adsorption

Adsorption is a process where an atom or a molecule is attached to the surface of a solid. Basically the bonding in adsorption is a quantum mechanical process similar to chemical bonding between atoms or molecules. In adsorption, however, one of the parties involved is a macroscopic medium with infinite number of electrons and usually with some kind of 2D symmetry. Adsorption is divided into two groups according to strength and nature of the bond between the adsorbate and the adsorbing material.

In physisorption the bonding is due to weak Van der Waals bonds. This is basically a dipole–dipole interaction where the adsorbate is attached to the surface as a molecule. The dipole–dipole interaction is formed since an atom or molecule has always some dipole character resulting from the electrons orbiting the nucleus. The interaction between the dipole and the surface may be understood by considering the dipole as two charges close to each other. The surface may then be replaced by similar image charges with opposite signs. The interaction is thus the force between two dipoles. The interaction of the dipoles induces a weak bond between the molecule and the solid. Far from solid, this force acts as $1/r^3$, until the wave functions of the interacting species begin to overlap. Overlapping of the wave functions causes a rapid increase in potential energy, thus a potential minimum is formed near the surface. The minimum is usually situated 3–10 Å from the surface with binding energy in the range of 5–100 meV. Comparing this to kinetic energy at room

temperature (kT≈25 meV), it can be seen that the physisorption is not very stable at room temperature and it can be studied only at low temperatures. Furthermore, physisorption is observed only if stronger chemisorption is not present, like in the case of noble gases on metallic surfaces. Since the binding energy of the adsorbate is low, the molecules adsorbed are quite mobile on the surface and may travel relatively long distances on the surface before desorption even in high temperatures. This is why physisorption often acts as a precursor state for chemisorption when appropriate adsorption site for chemisorption is not instantly found.

In chemisorption much stronger bond is formed. Physisorption is basically a physical reaction, whereas chemisorption can be considered as chemical bonding. The bond is either covalent or ionic in nature and it is formed in mixing of the interacting orbitals. The potential energy curve in chemisorption is quite similar to the curve in physisorption. The difference is that the potential minimum in chemisorption is closer to the surface and it is much deeper than in physisorption. The distance of a chemisorbed molecule from the surface is usually 1–3 Å and the binding energy of the molecule is several electron volts.

In chemisorption charge transfer usually takes place during the bonding thus the bonding highly affects to the electronic configuration in both the adsorbate and the substrate. The change in electron configuration may deform the molecule adsorbed and, if the deformation is large enough, eventually broke the molecule. In this case the adsorption is called dissociative, otherwise associative. Chemisorption is often dissociative, whereas physisorption is always associative.

Let us now consider, as an example, adsorption of a two atomic molecule, $X_2$, on a metal surface. Hypothetical potential curve, called Lennart–Jones-diagram, of the adsorption process is shown in fig. 2.1. The zero level of the energy is the potential energy of the free molecule far from the surface. The potential curves shown are: the long-dashed is Van der Waals (physisorption) potential and the short-dashed is the potential of molecule dissociated to two separate atoms (chemisorption). The separation of these curves at infinity equals the dissociation energy $E_{diss}$ of the molecule. The potentials intersect between the physi- and chemisorption minima thus between the minima there is a potential barrier with height $E_{act}$.

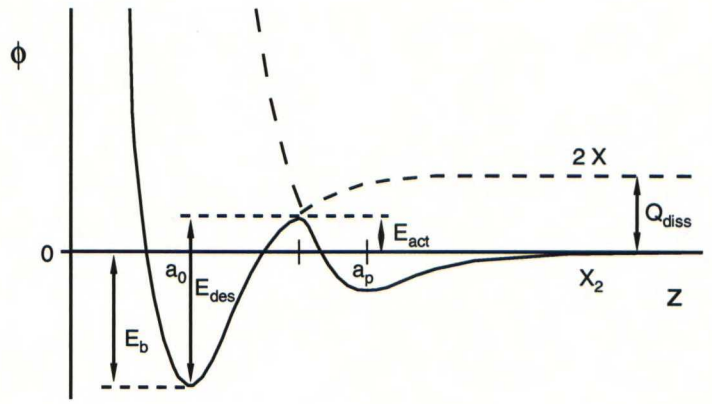


Figure 2.1. *Hypothetical potential curve of a two atomic molecule $X_2$ approaching the surface.*

Since range of electrostatic forces is much longer than the dimensions of electron orbitals, the molecule first starts to feel the Van der Waals force, when approaching the surface. The molecule approaches the surface until the physisorption minimum $a_p$ is achieved. Still approaching the surface there is a rapid potential increase. The molecule may desorb from the minimum at once of it may stay on the surface for a while moving along the surface as physisorbed molecule. If the molecule has enough kinetic energy, it can overcome the potential barrier and move closer to the surface. At the distance where the two potentials are equal it is advantageous to molecule to dissociate and fall to the chemisorption potential minimum $a_0$. This is only possible if there is a suitable adsorption site unoccupied at the location of the molecule. Since the molecule may move along the surface as physisorbed, it may find an adsorption site though the site where the molecule initially hit was occupied. The solid line in fig. 2.1 represents the potential of the whole adsorption process. The energy gained is the binding energy of the molecule $E_b$: the difference between zero and the chemisorption minimum. When desorbing from the surface, atoms adsorbed need energy $E_{des}$ to overcome the potential barrier. At the top of the barrier the atoms bind together again to form a molecule $X_2$. This molecule then escapes the surface along the Van der Waals curve. [16]

## 2.1 Adsorption kinetics

The amount of adsorbed species on the surface is usually described with coverage:

$$\theta_s = \frac{N}{N_s}, \tag{2.1}$$

where $N$ is the number of adsorbed molecules and $N_s$ the total number of possible adsorption sites on the surface. Often coverage is also defined as the ratio of the number of adsorbed molecules and the number of surface atoms on the substrate. These two ways of defining the coverage are proportional to each other and for convenience, in this work the coverage defined by this latter way is denoted by plain $\theta$, without the subscript s. Another important physical quantity in considering adsorption kinetics is the sticking coefficient S: It is the probability of adsorption of a molecule striking the surface and often dependent on coverage.

In order to understand adsorption kinetics we need to consider things that affect the sticking coefficient:

(i) Like in fig. 2.1, in many chemisorption processes there is a potential barrier $E_{act}$ which have to be overcame before chemisorption is possible. This means that only the molecules with kinetic energy above $E_{act}$ are able to adsorb. Hence the sticking coefficient have to be proportional to Boltzmann term "$\exp(-E_{act}/kT)$".

(ii) Many bonding processes are orientation dependent, thus the impinging molecule has to have particular orientation in respect to the dangling bonds of the surface atoms (steric factor). In addition, the site of impact affects to the sticking coefficient since the surface has different adsorption sites with different potentials. The mobility of the molecule is also of interest since high mobility increases the probability of finding a suitable adsorption site.

(iii) If the molecule collides elastically with the surface, it cannot be bound in adsorption minimum since it has too much kinetic energy and it desorbs after a very short period on the surface. This means that the incoming molecule has to transfer at least part of its kinetic energy to the substrate. Surface excitations, such as phonons and plasmons, are thus involved.

(iv) The number of remaining adsorption sites is also relevant since if the incoming molecule do not find a free site, it cannot adsorb. The less there are free sites the less particles adsorb. Precursor states, like physisorption, help in finding a free site since they increase the time spent and the distance diffused on the surface.

Taking into account these phenomena we may write [16]

$$S(\theta) = \sigma f(\theta_s) \exp(\frac{-E_{act}}{kT}), \tag{2.2}$$

where $\sigma$ is condensation factor taking into account effects of molecular orientation, energy losses, etc. $f(\theta_s)$ is the occupation factor describing the probability of finding a free adsorption site. For non-dissociative adsorption the site is either occupied or unoccupied, thus

$$f(\theta_s) = 1 - \theta_s. \tag{2.3}$$

For a two atomic molecule adsorbing dissociatively there has to be two free sites side by side, thus

$$f(\theta_s) = (1 - \theta_s)^2. \tag{2.4}$$

[16]

This is of course only a simple model for adsorption and real adsorption processes are much more complicated. For more detailed treatment of the adsorption readers are referred to [17, 18].

## 2.2 Interaction of adsorbed species

In considering the adsorption on surfaces, forces between the adsorbed species cannot be ignored. For low coverages, under a monolayer, the density of the adsorbed species is low thus single atoms or molecules may lay far from each other on the surface. If the temperature is high, the molecules have high kinetic energy and the adsorbed molecules are quite free on the surface. If this is the case, the molecules are randomly orientated on the surface and the phase can be considered as a 2D lattice gas. A schematic view of the lattice gas is presented in fig. 2.2(a).

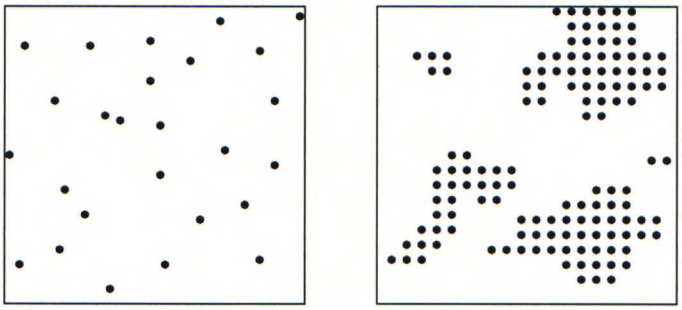

(a) 2D lattice gas (b) 2D solid islands

Figure 2.2. *Adsorbate phases on the surface: a) 2D lattice gas and b) 2D solid islands. Liquid phase is similar to b) with islands of molecules only internal long range order missing.*

Molecules with lower kinetic energy may interact with each other or with the surface more strongly and arrange in some ordered structure. If the molecules do not fill the whole space in favored structure, they may form islands with high density and empty spaces between the islands. Islands with long range order are shown in fig. 2.2(b). This phase can be considered as solid forming 2D crystallites. Newly adsorbed species usually adsorb on the edge of the crystallites. If these are islands with dense packing but with no internal long range order, the phase can be considered as 2D liquid droplets. Temperature variation can cause 2D phase transitions between these phases as in real 3D systems.

The ordered structure is either characteristic to the surface or to adsorbed molecules. Which symmetry the adsorbed overlayer obeys is dependent on the ratio of the strengths of the bonds between the molecule and the surface and between two adsorbed molecules. Usually the vertical forces between the adsorbed molecules and the surface are much stronger than the lateral forces between the molecules, hence the structure is usually related to the order of the surface.

The forces acting laterally between the adsorbed molecules are usually of four different nature or a combination of these [16]:

**Van der Waals interaction** is due to charge fluctuations in the molecule i.e. it is due to fluctuating dipole forces. This interaction is present in every adsorption system and it is not characteristic only for some type of the molecules. Van der Waals interaction is significant only for physisorbed inert gas atoms at low temperature since for most systems there are much stronger interactions present.

**Dipole forces** are related to permanent dipole moments in polar molecules like $H_2O$ and CO or to permanent dipole moments formed by charge transfer during the bonding of the molecule with the surface. Dipole forces may be either attractive or repulsive depending on the adsorption geometry.

**Orbital overlapping** leads to repulsive forces in densely packed adsorption layers. The dense the structure is the stronger is the repulsion. The ultimate lower limit of the distance between two adsorbed molecules is determined by orbital overlapping.

**Substrate-mediated interactions** have two origins: The electron configuration of the substrate is changed in the vicinity of the bond in strongly chemisorbed molecules. Accumulation or depletion of charge, ranged of a few Ångströms, may increase or decrease the interaction of a second adsorbate particle with the surface. These forces, although indirect, can be considered as interaction between adsorbate molecules. The other indirect interaction is due to elastic properties of the surface. Chemisorbed molecule may attract neighboring substrate atoms by strong charge rearrangement. Resulting local contraction of lattice must be compensated by an expansion of lattice at more distant points. Atom trying to adsorb to expanded region have to do more work in order to contract the lattice. This leads to either attractive or repulsive forces between molecules depending on adsorption geometry. Both indirect interactions are usually weaker than the dipole–dipole interactions.

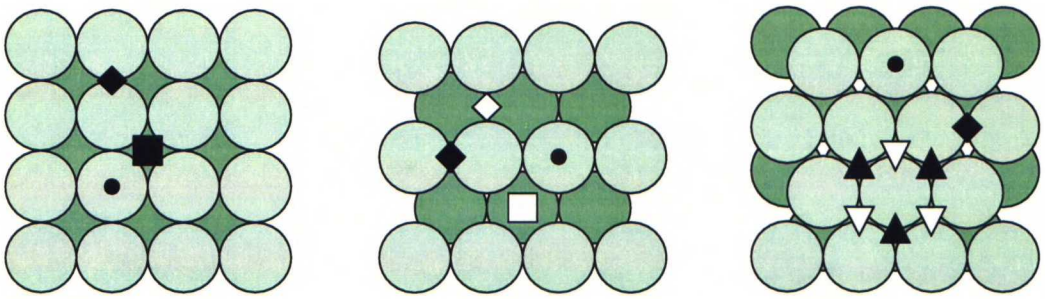

(a) fcc(100) (b) fcc(110) (c) fcc(111)

Figure 2.3. *High symmetry adsorption sites on low index fcc surfaces: a) fcc(100):* • *top,* ■ *4-fold hollow and* ♦ *bridge, b) fcc(110):* • *top,* □ *4-fold hollow,* ♦ *short bridge and* ◊ *long bridge. c) fcc(111):* • *top,* ♦ *bridge,* ▲ *hcp 3-fold hollow and* ▽ *fcc 3-fold hollow.*

## 2.3 Ordered adsorption structures

Since the lateral interactions are usually much weaker than the vertical interactions, the favored adsorption structure is often related to the structure of the substrate. The 2D adsorption structure may be dependent on both the vertical and lateral forces whereas the actual adsorption sites usually depend mostly on the substrate.

Let us now consider low index fcc surfaces as an example. In fig. 2.3(a) there is shown a fcc(100) surface. On the surface there are three different high symmetry adsorption sites available: a top site on top of the substrate atom, a 4-fold hollow in the hole created by four atoms and a bridge site between two atoms next to each other. On fcc(110) surface (fig. 2.3(b)) there is a asymmetric 4-fold hollow and two bridge sites (short and long) in addition to a top site. On fcc(111) surface, in addition to top and bridge sites, there is two different 3-fold hollow sites: a hcp site in the hole formed by three atoms with an atom in the next layer and a fcc site on similar 3-fold hole but the next layer atom missing. These 3-fold sites are similar to sites on hcp(0001) surface. In many cases the adsorption structure has dimensions, which allow all the adsorbed molecules to be on the same energetically favored site.

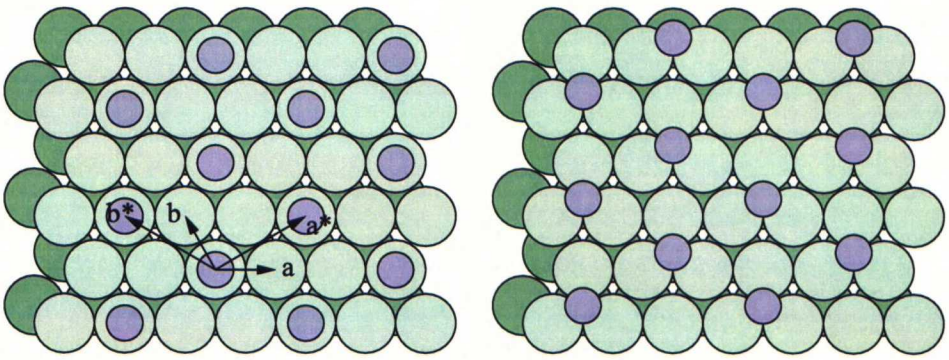


(a) p($\sqrt{3} \times \sqrt{3}$)R30° at top site (b) p($\sqrt{3} \times \sqrt{3}$)R30° at hcp site

Figure 2.4. *Two* $p(\sqrt{3} \times \sqrt{3})R30°$ *structures with different adsorption sites on hcp(0001) surface: Atoms are a) on top site and b) on hcp 3-fold hollow site.*

The regular 2D lattices have three possible lattice dimensions in comparison to the substrate lattice: If all the adsorbed atoms are on the same adsorption sites, the structure is called simple super lattice, in the case of periodic variation of adsorption sites the structure is called coincidence lattice and if there is not any periodicity in the adsorption sites, the lattice is incoherent. Another used characterization is division to commensurate (simple and coincidence) and incommensurate (incoherent) structures. In the Fig. 2.4 there is shown two commensurate ($\sqrt{3} \times \sqrt{3}$)R30° structures with different adsorption sites: In 2.4(a) all the atoms are on the top site and in 2.4(b) the atoms are on the hcp 3-fold hollow site.

Two different notations are used in expressing adsorption structures: The more common is the Wood notation used in fig. 2.4 and the more general is called a matrix notation. The Wood notation is of the form of

$$X(ijk) - p(|a^*| \times |b^*|)R\theta - NY,$$

Where X(ijk) describes the substrate (X is the chemical symbol) and the Miller indexes of the surface. p is for primary, that is one molecule in unit cell. Instead of p, a c is used if there is a center atom(s) in the unit cell. $|a^*|$ and $|b^*|$ are the lengths of the adsorbate cell vectors, shown in fig. 2.4(a), in the units of the substrate unit vectors. $\theta$ tells the rotation of the adsorbate structure corresponding to the substrate,

N is the number of molecules in the adsorbate cell and Y is the chemical symbol of the adsorbate. The Wood notation cannot be formed if the angle between the adsorbate unit vectors is not the same as the angle between substrate unit vectors, except for a few special angles, like rectangular adsorbate structure on hexagonal surface. However, since the adsorption structures generally replicates the symmetry of the substrate, using the Wood notation is possible in almost all cases. The exception is incommensurate structures, when only matrix notation is possible.

The matrix notation has some what simpler form than the Wood notation but the usage of it is more complicated. The matrix notation is constructed from the adsorption cell vectors by presenting them as linear combinations of substrate unit vectors. The matrix can be formed from

$$\mathbf{G}\begin{pmatrix} a \\ b \end{pmatrix} = \begin{pmatrix} a^* \\ b^* \end{pmatrix}, \qquad \text{where} \quad \mathbf{G} = \begin{pmatrix} n & m \\ p & q \end{pmatrix}.$$

For example the structure shown in fig. 2.4 with CO on Co(0001) can be expressed as

$$Co(0001) - p(\sqrt{3} \times \sqrt{3})R30° - CO$$

or

$$Co(0001) - \begin{pmatrix} 1 & 1 \\ -1 & 2 \end{pmatrix} - CO.$$

With matrix notation it is also possible to express incommensurate as well as commensurate structures.

# Chapter 3

# Spectroscopic methods

## 3.1 Low energy electron diffraction

Low Energy Electron Diffraction (LEED) is a technique frequently used in examining the quality of the single crystal sample. It also provides useful information on adsorbed adlayers and the relaxations of the surface layers caused by the adsorbate.

In LEED experiments an apparatus shown in fig. 3.1 is used. It consists of a hemispherical fluorescent screen with a radius of few centimeters, electron gun in the middle of the screen and two to four grids, $G_1$–$G_4$, in front of the screen.

There are two kinds of LEED systems available: The system where the diffraction pattern is observed from front side of the screen, FV–LEED (FV for Front View) and the system where the screen is transparent and the diffraction is observer from back side of the screen, RV–LEED (RV for Rear View). The weakness of the FV–LEED is that the sample and its holder screens partly the view. In RV–LEED the electron gun screens the center of the the view, but otherwise all the screen is visible. It is also easy to attach a camera for data collection to the system if RV-LEED is used.

The LEED apparatus in fig. 3.1 works as follows: Electrons accelerated by the electron gun hit the sample situated in the focus of the hemisphere and diffract towards

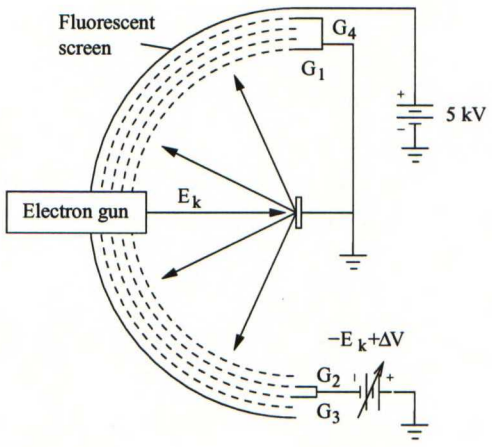


Figure 3.1. *A schematic view of the LEED apparatus.*

the screen. The sample is usually grounded as is the grid $G_1$. Thus a field free space is established between the sample and the $G_1$ through which the electrons travel to the sample and back after scattering. The grids $G_2$ and $G_3$ are biased to a negative potential $-E_k + \Delta V$. These grids prevent the inelastically scattered electrons passing to the screen thus suppressing significantly the background illumination. $\Delta V$ is of the order of few volts and it is adjusted so that the best contrast is achieved. Grids $G_2$ and $G_3$ are also used in focusing the diffraction pattern. Grid $G_4$ is also grounded in order to insulate the screen from the suppressing field produced by the grids $G_2$ and $G_3$. The fluorescent screen is biased in a high positive potential in order to accelerate the electrons to the screen. High kinetic energy of the electrons is needed since only the electrons with sufficient high energy can exite fluorescence on the screen.

Determination of the 2D surface structures of the sample and adsorbed adlayers with LEED is quite straightforward: The reciprocal of the structure on the surface is seen on the fluorescent screen. However, LEED pattern do not tel us directly the exact adsorption sites, the structure inside the unit cell and the bond lengths in third dimension. To achieve this information IV-analysis has to be used. In order to understand the methods behind the IV-analysis, physics of the scattering event has to be considered.

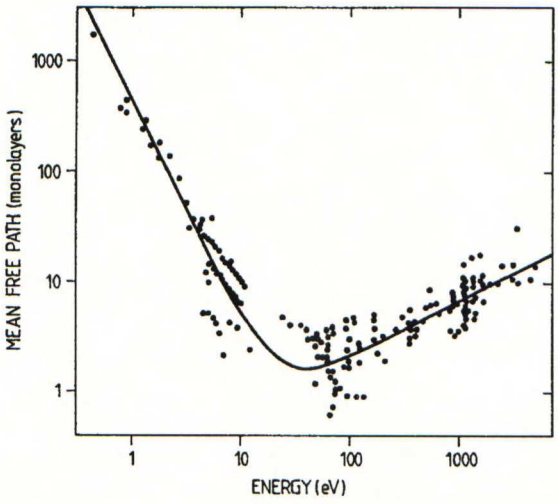


Figure 3.2. *Mean free path of electrons in solids as a function of kinetic energy. Points represent measured values in different materials. [19]*

### 3.1.1 Theory of electron diffraction

Electron energies used in low energy electron diffraction are usually in the range of 20–500 eV. From the fig. 3.2 can be seen that the mean free path of these electrons is only few atomic layers. Scattering of the electrons thus occurs on the topmost layers of the sample and the scattering can be considered as almost two dimensional. Since the de Brogglie wavelength can be calculated from

$$\lambda = \sqrt{\frac{\hbar^2}{2mE}} \tag{3.1}$$

$$= \sqrt{\frac{150.4}{E(eV)}}\ \text{Å} \qquad \text{(for electrons)}, \tag{3.2}$$

the corresponding wavelengths are 2.74–0.55 Å. This is of the order of the interatomic spacing in solids thus the electron diffraction has to be considered as interference of waves.

Electron diffraction is basically Bragg diffraction: Diffracted electrons interfere constructively only if the wave vector change in diffraction equals some reciprocal vector of the surface, i.e. $\mathbf{K} = \mathbf{k}' - \mathbf{k}$ must equal a vector in reciprocal lattice $\mathbf{G}$. Since the

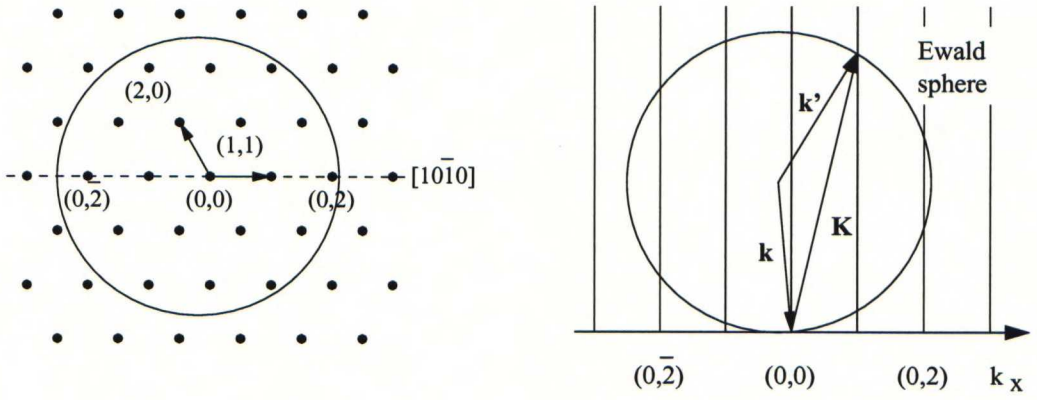


(a) Perpendicular to the surface (in [0001] direction).

(b) Parallel to the surface (in [10$\bar{1}$0] direction).

Figure 3.3. *Laue condition for 2D diffraction. Diffraction occurs in directions where the Ewald sphere crosses the rods.*

diffraction is now two dimensional, this can be written as

$$\mathbf{k}'_{||} = \mathbf{k}_{||} + \mathbf{G}_{||}. \tag{3.3}$$

where the subindex $||$ denotes the component of the vector parallel to the surface.

This can be illustrated by a Ewald construction. In 3D Ewald construction there is a 3D lattice of reciprocal points. In two dimensional case we can substitute the 3D lattice by a matrix of rods. Now we choose one rod as a center, i.e. point (0,0), and set the end point of the wave vector of the incoming wave to that point. Then we draw a sphere of radius $|\mathbf{k}|$ centering in the starting point of the vector. Resulted Ewald construction is shown in 3.3(a) and 3.3(b). The Laue condition $\mathbf{K} = \mathbf{G}$ is fulfilled whenever the Ewald sphere crosses a rod. The diffraction occurs in all directions inside the projection of the sphere in fig. 3.3(a). In 3.3(b) there is a cut along the [10$\bar{1}$0] direction and diffraction to (0,1) is shown. The length of the $\mathbf{k}$ is a function of energy thus the diffraction angle of the spots in 3.3 decreases and new spots appear to the margin of the sphere when the energy of the beam is increased.

This consideration is valid only in true 2D case. However, in LEED experiment the electrons scatter from few topmost atomic layers thus the third Laue condi-

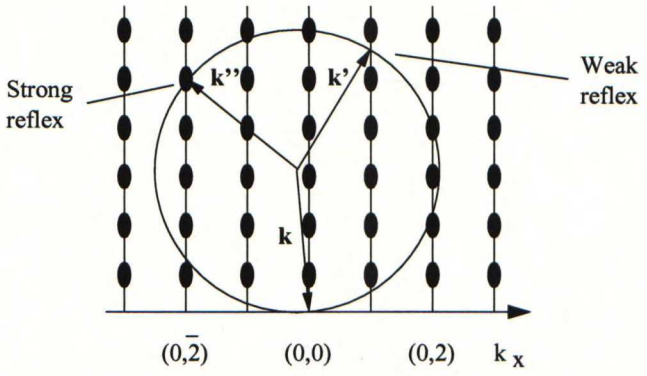


Figure 3.4. *Laue condition for quasi–2D diffraction. The thinner regions corresponds to weak reflection and the thicker regions to strong reflection.*

tion perpendicular to surface becomes significant. The scattering process in LEED experiments is more like something between 2D and 3D scattering.

Since the amount of electrons scattered beneath the surface decreases exponentially, the third Laue condition affects only weakly to the scattering. This quasi–2D diffraction can be illustrated with a modified 2D Ewald construction shown in fig 3.4. In the rods there are thicker and thinner regions which illustrate intensity variation in the diffraction spots. Thicker regions give rise to more intense diffraction than thinner regions. If the electrons would diffract evenly from all atomic layers trough the sample, the thicker regions would become points in 3D Ewald construction. The finite mean free path of the electrons therefore causes the intensity variation of the diffracted beams as a function of energy of the incident electrons. Analysing the intensity variations of the diffracted spots gives us useful information about 3D structure of the sample.

### 3.1.2 IV-analysis

In LEED–IV-measurement the intensities of diffracted spots are measured as a function of electron energy. The observed IV (intensity vs. voltage) -curves are then compared to the theoretically calculated ones. Fig. 3.5 illustrates measuring of a

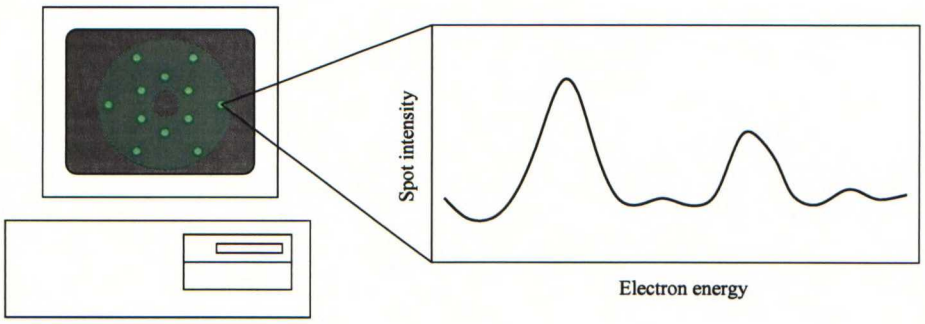


Figure 3.5. *IV-curves are collected by measuring the intensities of the diffracted beams as a function of electron energy.*

IV-curve.

Let us now consider a (0,0) beam IV-curve measured from Ni(100) as an example. The measured curve is shown in fig. 3.6 [20]. There is indeed some structure in the curve. Since in (0,0) beam electrons are backscattered 180°, constructive interference occurs when the distance 2d, traveled by the electrons scattered from second layer, is multiplicity of the wavelength

$$2d = n\lambda, \qquad n \in \mathbb{Z}_+. \tag{3.4}$$

Substituting 3.2 for the intensity maxima can be written

$$E = \frac{150.4n^2}{4d(\text{Å})^2} \quad \text{eV}. \tag{3.5}$$

Energies of the intensity maxima calculated by (3.5) for the (0,0) beam of Ni(100) are tagged by the arrows in fig. 3.6. The peaks in IV-curve are, however, in slightly lower energies than eq. (3.5) predicts. This is partly explained by potential inside the crystal. The inner potential is usually of the order of 10 eV. The incoming electron is thus accelerated by this potential before the scattering and electrons diffract with somewhat higher energy than the accelerating energy of the electron gun. Additionally the potential of the scatterer also affects to the energy of the peaks.

Potential inside the target explains only the shift to the lower energy, but not peak splitting and additional shoulders in the intensity peaks. This fine structure of the

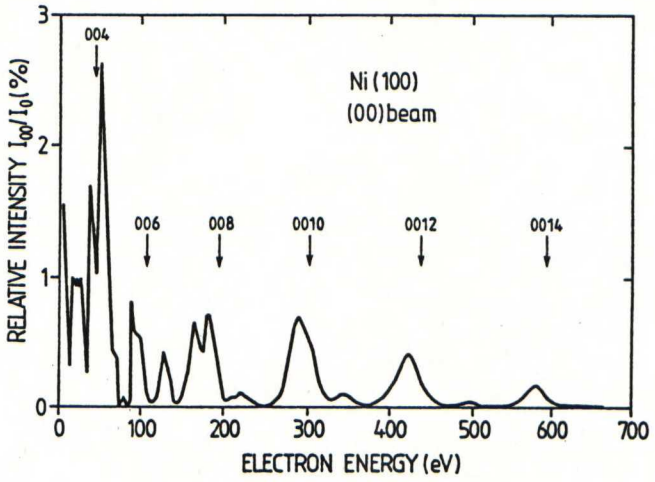


Figure 3.6. *IV-curve for the (0,0) beam of a clean Ni(100) surface. Diffracted intensity $I_{00}$ is referred to the intensity of the primary beam $I_0$. [20]*

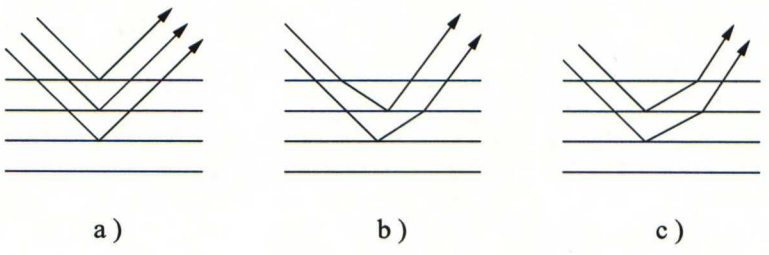


Figure 3.7. *Multiple scattering events: a) Only backscattering, b) Forwardscattering and subsequent backscattering, c) Backscattering and subsequent forwardscattering. [16]*

IV-curves is explained by multiple scattering events. Since the electrons interact strongly with matter, some electrons scatter more than once before leaving the substance. Fig. 3.7 presents some possible multiple scattering processes.

In IV-analysis the theoretical IV-curves are calculated for some possible atomic structure. Then the calculated curves are compared to the measured ones and the assumed structure is changed if needed. This is continued until the best fit is obtained. In the comparison of the measured and calculated curves so called reliability functions are used. The reliability functions take into account position, height and the width of the peaks, weighting the position since it depends strongly on the structure. Pedry's R-factor ($R_P$) is the most used reliability function. [16]

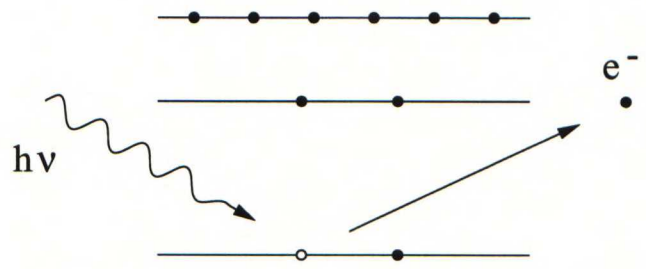


Figure 3.8. *The photoelectric effect: An electron absorbs the incident light quantum and the additional energy allows it to be freed. The excess energy is left as kinetic energy to the photoelectron.*

## 3.2 X-ray photoelectron spectroscopy

X-ray photoelectron spectroscopy (XPS) is a widely used technique in surface studies since it enables both the identification of the atomic composition on the surface and the distinguishing of the chemical state of the elements present. In addition it is surface sensitive, since the mean free path of the photoelectrons is of the order of Ångströms.

In an XPS experiment the sample is irradiated with X-rays and the amount of emitted photoelectrons is measured as a their function of kinetic energy. Every atom, except hydrogen and helium, has a specific XP spectrum from which the composition of the surface and the chemical state of the elements can be determined.

### 3.2.1 Theory of photoelectron spectroscopy

XPS is based on the photoelectric effect explained by Einstein 1905 [21]: An electron bound to e.g. an atom absorbs the energy of a light quantum and if the energy of the quantum absorbed was sufficient to overcome the binding energy of the electron, it escapes from the atom and the remaining energy is left to electron as kinetic energy. Fig. 3.8 illustrates the photoelectric effect.

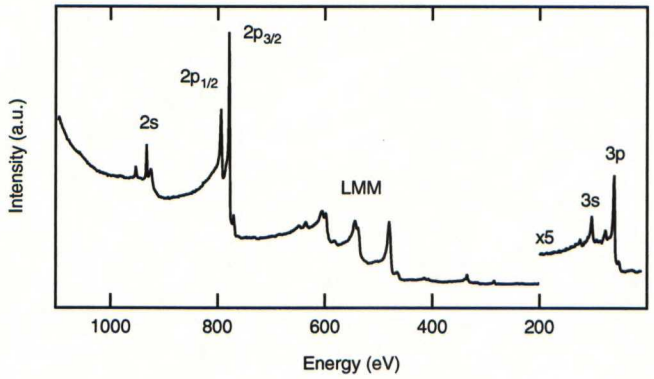


Figure 3.9. *XP spectrum of a clean Co sample. The tagged peaks corresponds to the core level photoelectron peaks and LMM auger transition peaks.*

The energy left to photoelectron originated from a solid has to be corrected by the work function of the material, since the binding energies of the electrons are referred to the Fermi surface. Thus the kinetic energy $E_{kin}$ of the photoelectron is

$$E_{kin} = h\nu - E_b - \phi, \tag{3.6}$$

where $E_b$ is the binding energy, $h\nu$ the energy of the light quantum and $\phi$ the work function of the material.

In the XPS measurements the energy of the incident X-ray beam is known and the binding energy of the emitted electrons can be calculated from

$$E_b = h\nu - E_{kin} - \phi_s, \tag{3.7}$$

where $\phi_s$ is the work function of the spectrometer.

The XP spectrum measured from the clean cobalt surface is shown in fig. 3.9. The spectrum is usually presented reversed and the measured energy range is typically 10–1100 eV. Cobalt core level photoelectron peaks can be distinguished from the spectrum in addition to LMM auger transition peaks [22]. The rising background is due to inelastically scattered electrons.

### 3.2.2 Experimental setup

In XPS measurements characteristic X-rays are widely used. Common anode materials are Mg and Al. The energies of the characteristic X-ray lines are 1253.6 eV for Mg $K_\alpha$ radiation and 1486.6 eV for Al $K_\alpha$ radiation.

The X-rays are produced by colliding accelerated electrons with the anode material. In the collision both bremsstrahlung and characteristic X-rays are produced. However, the intensity of the characteristic lines are much higher than the intensity of the continuous bremsstrahlung background. This way a very high intensity of radiation is achieved. The drawback of the high intensity is the needed water cooling of the anode. Very often a dual anode X-ray gun, with both Mg and Al anodes, is used.

Since the linewidths of the characteristic emission lines are several hundred meV, it is necessary to use a monochromator to obtain resolution high enough for the high accuracy analysis of chemical shifts. This was, however, not the case during this study.

Synchrotron radiation can also be used in XPS studies and it has come an important source of X-rays lately. Synchrotron radiation is advantageous, since it has a continuous spectrum and thus it is possible to use various energies of the radiation. [16]

Photoelectrons are usually analysed with a hemispherical analyzer (HSA) or a cylindrical mirror analyzer (CMA). HSA was used in XPS measurements during this work.

A hemispherical analyzer is sketched in fig. 3.10. The HSA operates as follows: Electron beam coming to the analyser travels first through a lens system were it can be decelerated and focused. After the lens system, the photoelectrons fly between two metallic hemispheres set to different potentials. The potential difference between the hemispheres determines the kinetic energy of the electrons passing the analyzer. Fast electrons collide the outer and slow electron the inner hemisphere. Only electrons with specific energy pass to the detector and contribute to the spectrum.

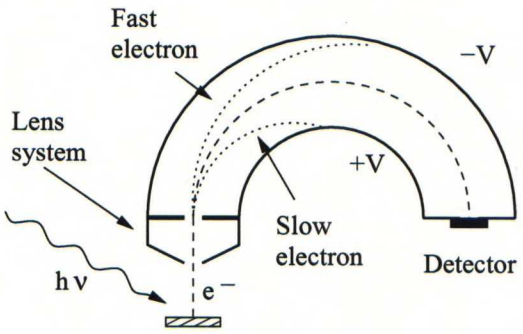


Figure 3.10. *Hemispherical analyzer. Electrons are decelerated and focused in the lens system and the electrons with specific energy are filtered with the hemispheres at different potentials.*

HSA can be used in two modes: constant $\frac{\Delta E}{E}$ -mode and constant $\Delta E$ mode. First is obtained by scanning the potential difference between the hemispheres and the second by keeping the potential difference between the hemispheres constant and scanning the retarding voltage of the lens system. During the XPS measurements the HSA was used in constant $\Delta E$ mode. [16]

# Chapter 4

# Experimental

Many techniques used in surface studies use electrons or ions as probes. The inelastic mean free path of these probes has to be considered if the energy of the probing particles is of importance. In atmospheric pressures the mean free path of these particles is considerably smaller than the dimensions of the measuring equipment, hence lower pressures have to be used. Pressures in High Vacuum (HV) range, i.e. under $10^{-6}$ Torr (1 Torr $\widehat{=}$ 133 Pa), are sufficient to fulfill the requirement of long mean free paths.

This pressure, however, is not low enough for surface studies, since in the HV range the impinging rate of the molecules to the surface of the sample,

$$Z = \frac{p}{\sqrt{2\pi m k_B T}} , \tag{4.1}$$

is of the order of $10^{15}$ collisions/cm$^2$s. Assuming unity sticking coefficient and surface density of $10^{15}$ atoms/cm$^2$, one monolayer is adsorbed in 1 s at $10^{-6}$ Torr. This results to very rapid contamination of the sample and the surface cannot be considered as clean. Contamination of the surface is avoided by using considerably lower pressure, called Ultra High Vacuum (UHV), range, where the pressure is around $10^{-10}$ Torr. In UHV the composition of one monolayer takes few hours and the cleanness of the sample can be maintained during measurements.

In this work the measurements were performed in a stainless steel UHV chamber

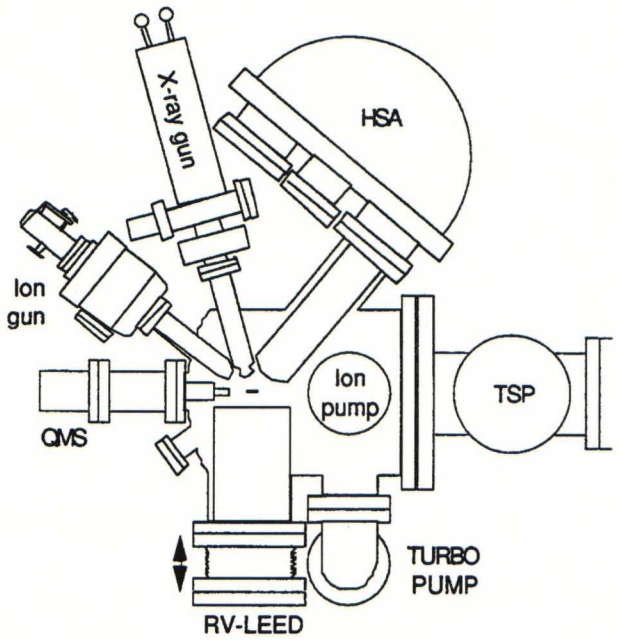


Figure 4.1. *Top view of the UHV chamber and the equipment used during this work [23].*

with a base pressure of $2 \times 10^{-10}$ Torr. Top view of the chamber with some of the equipment mounted is sketched in fig. 4.1. The chamber was pumped with a 400 l/s ion pump and a titanium sublimation pump. During gas dosing and after opening the chamber pumping was performed with a 150 l/s turbomolecular pump backed with a mechanical pump. A mechanical pump was also used in roughing the chamber and the gas lines. The pressure in the chamber was monitored by a hot cathode ion gauge.

Now and then the chamber had to be opened for maintenance and after bringing it up to atmospheric pressures it had to be baked at 500K for at least 24 hours to get rid of the species, e.g. water, adsorbed to the walls of the chamber during the maintenance. Baking increased the desorption rate of the adsorbed species and allowed lower pressure to be achieved in considerably shorter time. After the chamber had cooled down after baking the pressure was already in the range suitable for measurements whereas without baking this would take several weeks.

With the equipment several techniques, common in surface studies, could be used:

XPS, LEED, TDS (Temperature Programmed Desorption) and EELS (Electron Energy Loss Spectroscopy), mentioning only a few.

Several instruments, needed during measurements, were mounted to the chamber. They all were in the same plane perpendicular to the z-direction and had the same focus in the center of the chamber. The orientation of the devices is shown in fig. 4.1. A differentially pumped ion gun was used during sputtering, a dual anode X-ray gun, with Mg and Al anodes, and a hemispherical analyser in XPS measurements, a QMS (Quadrupole Mass Spectrometer) for residual gas analysis and a RV-LEED in electron diffraction experiments.

In addition to devices directly contributing the measurements, there were also a xyz$\theta\phi$-manipulator for the sample manipulation and several leak valves for the gas introduction mounted to the chamber. The manipulator had also power, thermocouple and piping feedthroughs needed for heating, temperature measurement and cooling. The sample holder attached to the manipulator could be cooled by pumping liquid nitrogen through the piping inside the holder.

## 4.1 Substrate

### 4.1.1 Structure of a hcp(0001) surface

The atomic structure of a hcp crystal is presented in fig. 4.2(a). In a hcp crystal there are hexagonal close packed layers on top of each other. The indexing of hcp crystals contains four indexes. The orientation of the indexes is also presented in fig. 4.2(a): The three first ones (X, Y and W) are in the hexagonal plane rotated 120° corresponding to each other. The sum of these three indexes has to be zero. The fourth index Z is perpendicular to the plane aligned by the first three indexes.

The (0001) surface, depicted in fig. 4.2(b), is thus the hexagonal close packed plane of the hcp crystal. In hcp and fcc crystals subsequent layers are aligned so that the atoms of the next layer are in 3-fold sites of the previous layer. The difference between hcp and fcc is that in a hcp crystal there is only two different kind of layers

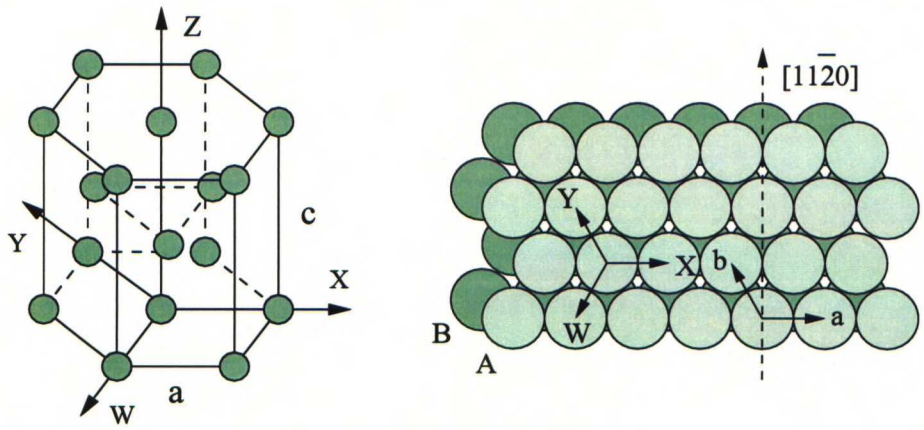


(a) Atomic structure of a hcp lattice.

(b) Co(0001) surface structure.

Figure 4.2. *The structure of the sample. Lattice constants: a=2.51 Å and c=4.07 Å.*

(marked A and B in fig. 4.2(b)) stacked in the sequence ABAB..., whereas in a fcc structure there is three differently positioned layers (usually marked A, B and C). In the hcp(0001) surface this means that there is transparent cites on the crystal which are missing from the fcc(0001) surface. The transparent cites are easily seen in fig. 4.2(b). The (0001) surface has a 3-fold rotational symmetry and a mirror plane along [11$\bar{2}$0], thus it belongs to the point group 3m. [16, 24]

The indexing on the hcp(0001) surface is usually carried out by two lattice unit vectors (a and b in fig. 4.2(b)) rotated 120° to each other.

### 4.1.2 Co(0001)

The cobalt sample, with a nominal purity of 99.999 %, had a hexagonal close packed surface. The diameter of the sample was 11 mm and it was spot welded to tantalum wires attached to the sample holder. The holder was a part of the $xyz\theta\phi$ manipulator which allowed the sample to be rotated around its own axis in addition to rotation and movement of the whole manipulator.

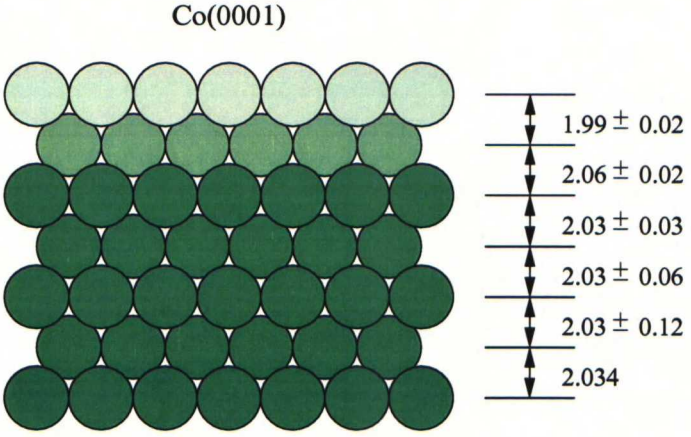


Figure 4.3. *Side view of the Co(0001) surface in [10$\bar{1}$0] direction. Distances (Å) between the atomic layers calculated in [25] are included. Relaxation of the two uppermost atomic layers is evident.*

The sample could be heated resistively by conducting current via tantalum wires and cooled by heat conduction via a copper wire to the liquid nitrogen cooled sample holder. With these methods the temperature range of the sample was 160–693 K, where the low temperature side was limited by the heat conduction from the sample and the high temperature side due to cobalt's phase transition from hcp to fcc at 693 K.

The sample has been in use for a while and its structure has previously been determined by a LEED–IV-analysis [25]. The resulting 3D structure of the sample is presented in fig. 4.3. The distance between neighboring atomic layers in bulk is 2.034 Å and in [25] a relaxation of the two uppermost atomic layers were detected: Differences to the bulk values were $\Delta d_{12} = -0.04 \pm 0.02$ Å and $\Delta d_{23} = 0.03 \pm 0.02$ Å, where the subscripts denote the atomic layers. Distances between other layers were equal to the bulk value.

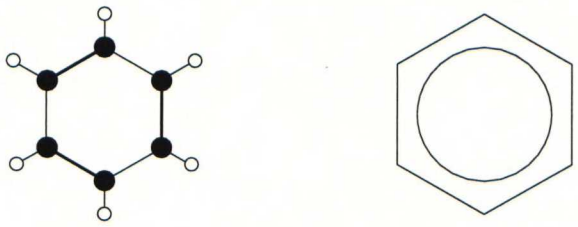

Figure 4.4. *Atomic structure of a benzene molecule (left) and drawing symbol of benzene in chemical compounds (right). The bond lengths in benzene are:* $d_{C-C}$*=1.40 Å and* $d_{C-H}$*=1.08 Å [26].*

Table 4.1. *Some physical properties of benzene.*

| Property | Symbol | Value | | Ref. |
|---|---|---|---|---|
| Atomic weight | M | 78.11 | amu | [26] |
| Diameter | d | 6.72 | Å | [27] |
| Density (293 K) | $\rho$ | 0.88 | g/mol | [26] |
| Melting point | m.p. | 278.5 | K | [26] |
| Boiling point | b.b. | 353 | K | [26] |
| Vapor pressure (300 K) | p | 1300 | Pa | [26] |

## 4.2 Benzene

Benzene, $C_6H_6$, is composed of six carbon molecules settled in a shape of a ring and of additional six hydrogen atoms each bind to a separate carbon atom. The atomic structure and commonly used drawing symbol of a benzene molecule are depicted in fig. 4.4. Some of the physical properties of benzene are presented in table 4.1.

Benzene, with a nominal purity of 99.5 %, used in the experiments was in a glass container attached to a gas line. Gaseous benzene vaporized in the line was purified with several freeze–pump–thaw cycles: The benzene was frozen with liquid nitrogen and the gas line was pumped. After pumping the benzene was thawed and boiled. This cycle was repeated until the benzene vapor in the gas line was pure enough. Gaseous benzene was introduced to the chamber through a leak valve and the purity was checked now and then with QMS.

## 4.3 Measurements

The aim of the measurements was to measure the IV-curves of the diffraction beams if possible and to determine the adsorption structures of benzene on Co(0001) from the measured curves.

### 4.3.1 Sample preparation

Before each measurement the sample had to be cleaned. The main impurity of the sample was carbon in addition to gases adsorbed from the residual gas in the chamber. The removal of adsorbed species was easy, since the main species, CO and hydrogen, desorbed when heated.

The removal of carbon was somewhat awkward since the carbon on the surface was originated from bulk carbon impurities and it did not desorb easily. In order to remove carbon species from the surface, the sample was bombarded with 1 kV argon ions produced by ion gun. This procedure is called sputtering and it is a common

way to clean metallic samples in vacuum. The noble gas ions were chosen since they do not react chemically with the sample. During sputtering the high energy ions collide with the atoms on the surface of the sample and remove them to the vacuum. The required sputtering times were approximately two to three hours.

The disadvantages of the sputtering process are that the sputtering causes some argon atoms to be embedded into the sample and the surface of the sample is left in disordered state after sputtering. This is why the sample had to be annealed after the sputtering. In annealing the temperature of the sample is raised slowly to high temperature. In this case the annealing temperature was 650 K, since higher temperature was not possible because of the phase transition at 700 K. The raising of the temperature was started during the sputtering. During the annealing the crystallinity of the surface of the sample was reordered and embedded argon atoms were removed. The annealing time is always a compromise between the well ordered surface and the impurity level since during annealing carbon diffuses from the bulk to the surface causing contamination. Well ordered Co(0001) surface with an acceptable carbon impurity level required annealing for an hour.

The impurity level of the sample was checked with XPS after annealing and if the sample was not clean enough the sputtering and subsequent annealing was repeated.

If the experiment was planned to be done at room temperature, the sample was simply let to cool down after annealing and the measurements were made after the sample had cooled to room temperature. If, on the other hand, the experiment was intended to be done under 300 K, the cooling of the sample holder with liquid nitrogen was started during annealing. This resulted to fastest possible cooling of the sample after annealing. During the cooling, hydrogen and other gases in the chamber may have adsorbed on the cold surface of the sample. To remove these species the sample was heated quickly to 500 K after the sample had achieved the desired temperature. After the quick heating, the sample cooled to measuring temperature in a few minutes, in which time the doses from the residual gas were negligible, and the sample was ready for measurement.

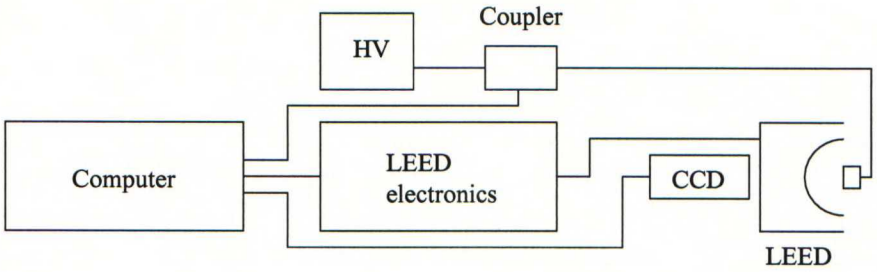


Figure 4.5. *Structural diagram of the LEED system.*

### 4.3.2 Preparation of an ordered adsorption structures

Before recording IV-curves, an ordered absorption structure had to be prepared: When the the sample had been cleaned and cooled to intended temperature, the dosing of benzene was done. The dose is usually measured as Langmuirs which are defined as the pressure times the exposure time, thus the dose is proportional to the number of the collisions of gas molecules to the surface of the sample. One Langmuir corresponds to 1 s at $1 \times 10^{-6}$ Torr.

After dosing the LEED pattern of the sample was verified and a snapshot of it was taken by a CCD camera for later analysis. If the diffraction pattern was the right one and good in quality the next step, recording of the IV-curves, could be made. However for the recording of the IV-curves the pattern had to be sharp with a wide energy range and if not, the preparation of the sample and the adlayer had to be done again.

### 4.3.3 Collection of IV-data

In IV-measurements the intensities of diffracted beams are measured as a function of incident beam energy. Before the measurement, the sample was cleaned and a wanted structure prepared. After a sharp diffraction pattern had been detected, the computer controlled data acquisition system was activated and the system took au-

tomatically care of the parameter adjust and the data collection. Structural diagram of the system is presented in fig. 4.5.

The data was collected by a CCD camera attached to the system. The camera was a black and white digital video camera with a resolution of 682×582 pixels. Though the diffraction pattern on the screen was green a b/w camera was used since it offers one significant benefit compared to color cameras: Since the actual picture is green, only one third of the pixels are in use in color camera whereas in b/w camera all pixels contribute to the picture, giving rise to a brighter picture with better contrast. The pictures were digitized by a capturing board attached to computer. Digitized pictures with a resolution of 512×512 pixels were saved for later analysis.

During the measuring the acceleration voltage was raised in steps and after each step a picture from the diffraction pattern was saved, resulting a series of pictures from which the IV-curves could be collected in off line analysis. Recording a picture to the memory of the data collection board took only a fraction of a second but the saving of the picture to the hard drive and chancing the acceleration voltage took couple of seconds. Long waiting times, before the next picture could be taken, lead to unnecessary electron radiation, which could cause erosion of the sample. In order to prevent the disordering and erosion of the adlayer caused by electron bombardment, the sample was biased to a negative potential higher than the acceleration potential during the saving of the picture and the parameter adjust. The bias voltage prevented the electrons hitting the sample between taking the pictures thereby shielding it. The biasing was controlled by the computer and it made possible to measure wider energy ranges at once since the sample was exposed to the electron beam only a fraction of the total time needed for a measurement.

The data collection and the operating of the LEED electronics with computer is described in detail elsewhere [28].

Before data collection the sample was aligned manually such that the maxima of the diffracted intensity appeared at the same energy in each of the symmetry equivalent beams. This assured that the sample was electrostatically perpendicular to the electron beam. Then the diffraction pattern was recorded in short parts overlapping at least 10 eV each other. The whole range could not be measured at once since, despite

of the shielding potential, the quality of the diffraction pattern grew worse during measuring. Several parts could be measured from the same, freshly prepared surface since the sample could be moved so that the electron beam hit to an undisturbed part on the surface. After some measurements the surface had to be prepared again.

# Chapter 5

# Benzene on Co(0001)

The studies of benzene adsorption on Co(0001) were started by K. Habermehl-Ćwirzeń. She determined the type of the adsorption as well as the coverage of saturated benzene at room temperature with TDS (Thermal Desorption Spectroscopy). Additionally she studied the work function chances induced by benzene adsorption.

## 5.1 Adsorption of benzene

In fig. 5.1(a) TD spectra of hydrogen originating from adsorbed benzene at various coverages are shown. Benzene was initially adsorbed at 300 K. The heating rate was 2.6 K/s. The desorption of hydrogen starts at 340 K. At all coverages TDS yields a broad hydrogen peak with a desorption maximum at 390 K, which is followed by a tail at the high temperature side. The fig. 5.1(b) shows the uptake curve of benzene on Co(0001) at 300 K. The uptake curve was obtained by integrating the area under the TD spectra and plotting it against the exposures. The saturation coverage was determined to be around 30 L. Additional C1s measurements with XPS gave the same value for saturation.

In TDS measurements no desorption of hydrocarbon fractions originating from benzene molecules were registered and the desorption of benzene (mass 78) was negligi-

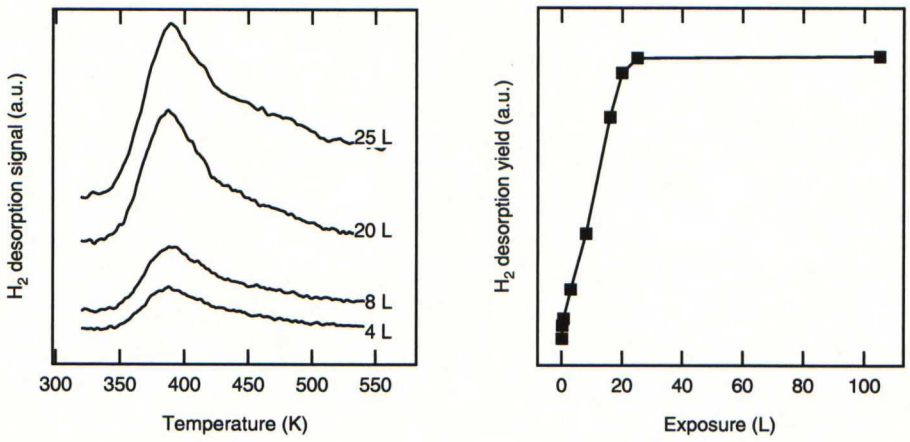


(a) $H_2$ desorption signal (b) $H_2$ desorption yield

Figure 5.1. *Hydrogen desorption from the sample: a) Thermal desorption spectra after exposing a clean Co(0001) surface to benzene. b) Integrated area of the desorption curve as a function of exposure. The solid line is drawn to guide the eye. [15]*

ble. Only the desorption peak of hydrogen was observed. The desorption measurements indicated that benzene on Co(0001) partially dissociated around 340 K. While hydrogen desorbed the hydrocarbon fragments remained at the crystal surface. This agreed with the XPS results, which showed no change on the carbon coverage before and after heating.

By knowing the coverage from the LEED experiments (see section 5.2 and comparing the $H_2$ desorption peak with that of $D_2$ on Co(0001) [29] it could be estimated that only one hydrogen per benzene molecule is desorbed. This loss suggests that with increasing temperature an intermediate, possibly $C_6H_5$, is formed. Such a process was already suggested for Os(0001) [30] and Co(10$\bar{1}$0) [31, 32]

With increasing coverage there is no temperature shift visible in the desorption-peak maximum. Therefore a second order process can be ruled out and a first order process has to be considered. The first-order behavior of the TDS data suggests that the decomposition process might be the limiting step of the desorption. The

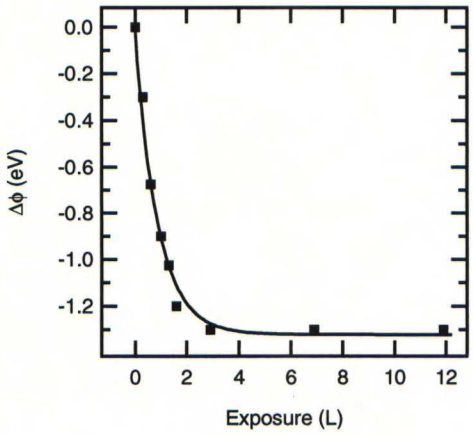


Figure 5.2. *Benzene induced work function change: Work function drops 1.3 eV as a consequence of charge transfer from benzene molecules to cobalt. The solid line is drawn to guide the eye. [15]*

activation energy of the decomposition was estimated to ~102 kJ/mole, assuming the prefactor to be $10^{-13}$ $s^{-1}$. This value is almost the same as suggested for the dehydrogenation of benzene on Co(10$\bar{1}$0) [32].

Fig. 5.2 shows the dependence of the work function of Co(0001) of the benzene exposure at 160 K. The work Function was measured by monitoring the cutoff energy of the photoelectron spectrum. At small exposures the change in the work function decreases linearly until it reaches the minimum of -1.3 eV. Using the value of 5.55 eV for the work function of clean cobalt [33], the saturation with benzene results in a work function value of 4.25 eV. By using the Helmholtz equation the dipole moment was estimated to 1.9 Debye/molecule.

The work function decreases due to partial charge transfer from the benzene molecules to the cobalt. After reaching the minimum $\phi$ stays constant indicating that forces between the adsorbed molecules do not change the bonding to cobalt. The value of -1.3 eV fits well to measured work function changes of other transition metals, like -1.2 eV for Ni(111), -1.52 eV for Pt(111) and -1.82 eV for Ru(0001) [14].

## 5.2 Adsorption structures

Adsorption phases were determined by investigating the LEED patterns after dosing to various amounts of benzene at various temperatures. As a result two different LEED patterns were observed. The patterns are shown in fig. 5.3: On the left there are the experimental patterns and on the right schematic views of the expected spots. In the schematic pictures the filled circles represent integral order spots and the open symbols fractional order spots. The different symbols indicate different domains on the surface.

The pattern in fig. 5.3(a) was observed at room temperature and it was easily reproduced over a wide range of exposures from 2 L up to 30 L. This structure was also detected under 270 K with low exposures. LEED pattern shown in fig. 5.3(a) follows from a

$$c(2\sqrt{3} \times 4)rect \qquad \text{or} \qquad \begin{pmatrix} 3 & 2 \\ -1 & 2 \end{pmatrix}$$

structure with three domains. A schematic view of the structure is shown in fig. 5.4(a). The top cite of the adsorbate molecules is just a guess since investigation of the LEED pattern does not tell the exact adsorption site and the molecules may as well lay on some other site than shown in fig. 5.4(a). Also the orientation of the benzene molecule may be different from fig. 5.4(a).

This structure gives a saturation coverage of $\theta_{ideal} = 0.125$. Comparing the C1s peaks detected from saturated $c(2\sqrt{3}\times 4)rect$—$2C_6H_6$ overlayer and the C1s peak detected from saturated $p(\sqrt{3} \times \sqrt{3})$—CO overlayer on Co(0001), with known coverage of $\theta = 0.33$ [34], the coverage of $\theta = 0.12 \pm 0.01$ is obtained. The ideal coverage of $\theta_{ideal} = 0.125$ corresponds to $\theta = 0.75$ carbon atoms for each cobalt atom on the surface.

The second pattern, shown in fig. 5.3(b), was observed below 270 K and with a little higher exposures. Exposures as high as 50 L still produced a nice LEED pattern. Corresponding adsorption structure is

$$p(\sqrt{7} \times \sqrt{7})R19.1^\circ \qquad \text{or} \qquad \begin{pmatrix} 3 & 1 \\ -1 & 2 \end{pmatrix},$$

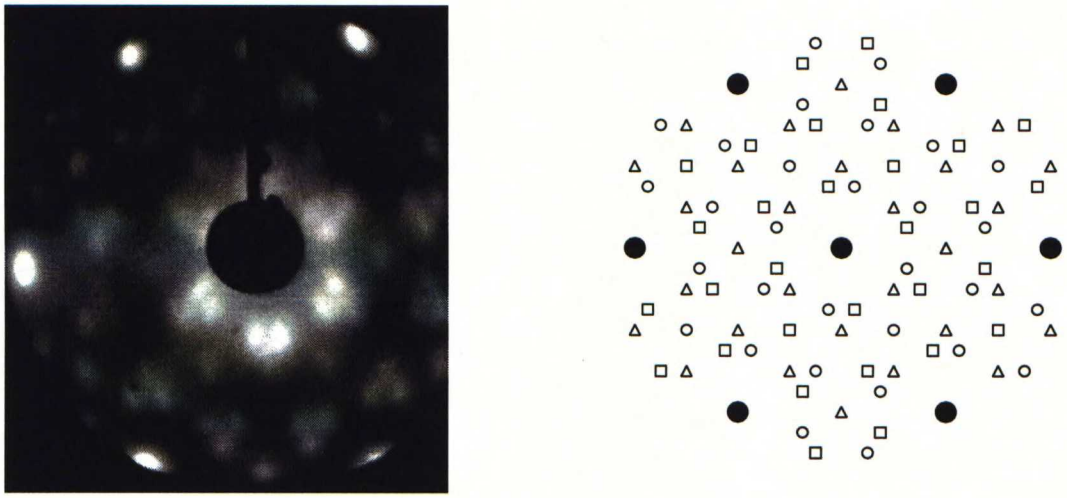

(a) $c(2\sqrt{3} \times 4)rect$

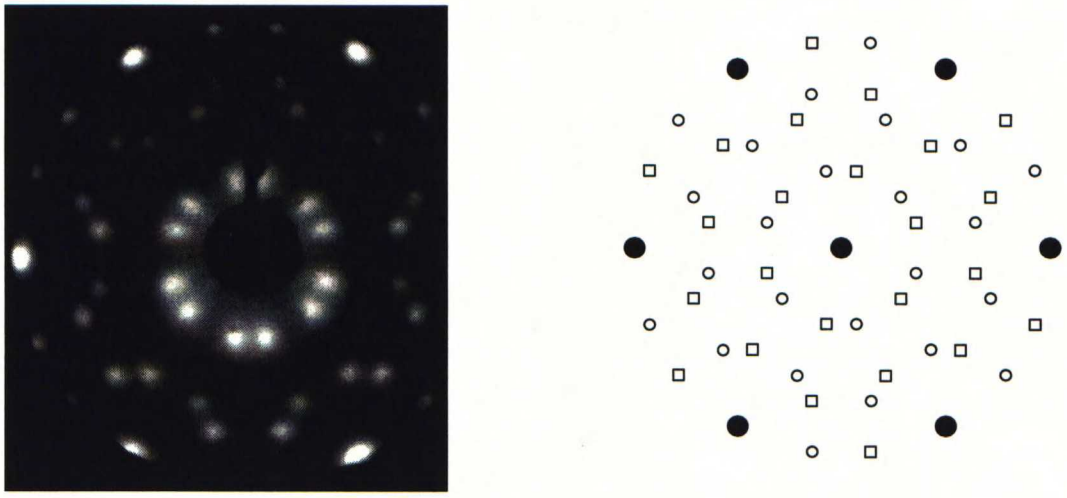

(b) $p(\sqrt{7} \times \sqrt{7})R19.1°$

Figure 5.3. *Observed (left) and schematic (right) LEED pattern of a)* $c(2\sqrt{3} \times 4)rect$ *(66 eV) and b)* $p(\sqrt{7} \times \sqrt{7})R19.1°$ *(68 eV) structure. The schematic LEED patterns show the spots expected within the circle defined by the first integral order spots in approximately the same orientation as in the observed patterns. Filled circles represent integral order spots and open symbols fractional order spots: different symbols indicate different domains.*

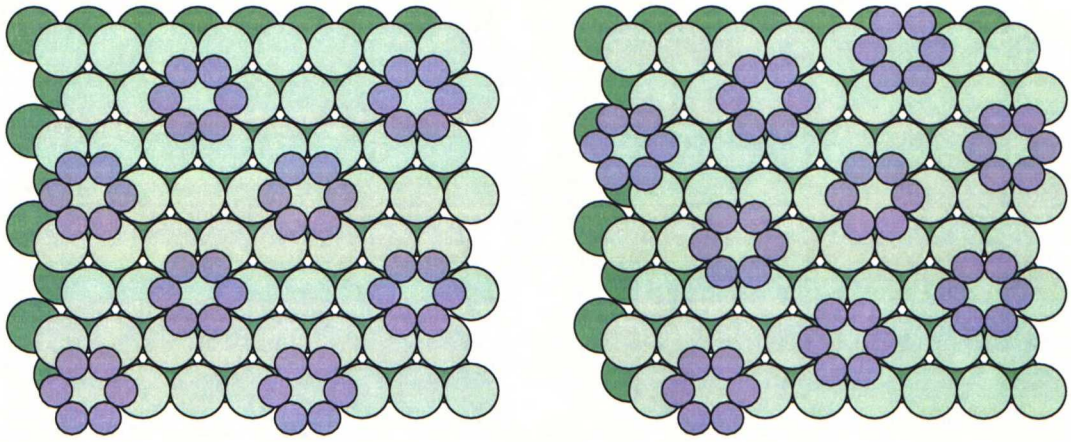

(a) $c(2\sqrt{3} \times 4)rect$ (b) $p(\sqrt{7} \times \sqrt{7})R19.1°$

Figure 5.4. *Observed adsorption structures of benzene on Co(0001): a)* $c(2\sqrt{3} \times 4)rect$ *and b)* $p(\sqrt{7} \times \sqrt{7})R19.1°$. *The coverages are* $\theta = 0.125$ *and* $\theta = 0.143$ *respectively. Adsorption cite and orientation of benzene molecules are chosen for simplicity purposes only. The real cite and orientation may differ significantly from those in figure.*

with two domains. A schematic view of the structure is represented in fig. 5.4(b). A detailed IV-analysis of the adsorption site, orientation of the molecule, bond length, and so on follows in the next sections for this structure.

The ideal coverage of the $p(\sqrt{7} \times \sqrt{7})R19.1°$ structure is $\theta_{ideal} = 0.143$ with a one molecule per unit cell. Determining the absolute coverage gave somewhat contradictory results: The comparison to the known $p(\sqrt{3} \times \sqrt{3})$—CO structure gave a coverage of $\theta = 0.28 \pm 0.04$. This suggests that there are two benzene molecules in unit cell thus the structure would in fact be $c(\sqrt{7} \times \sqrt{7})R19.1°$—2 $C_6H_6$. On the other hand, analysis of the measured IV-curves (section 5.4) suggested that there is only one molecule in unit cell: The calculation with two molecules resulted in considerably higher R-factors than calculation with only one molecule in unit cell. In addition, almost all references found [1, 2, 3, 5, 7, 6, 8, 35] conclude that there is only one benzene molecule in unit cell in $(\sqrt{7} \times \sqrt{7})R19.1°$ structure on hexagonal close packed surfaces. In the end all these refer to [35, 36] or [6]. References [35] and

[36] base their result to coverage calibration performed with deuterium and [6] to the fact that the benzene molecule occupies so much space that there can be only one molecule per unit cell. Only Lehwald et al. [37] suggested in the late 70's that there might be two molecules in unit cell.

The diameter of the benzene molecule in gas phase is 6.72 Å [27] and the lattice constant of cobalt is 2.51 Å. Thus the separation of two benzene molecules on the surface is only 6.64 Å. This suggests that there cannot be a fourth benzene molecule in the triangle formed by three molecules.

The size consideration and the results from the IV-analysis clearly states that there is only one molecule in unit cell despite of the inconsistent results obtained with XPS.

Both of the observed adsorption structures were also found during the adsorption of benzene on Ru(0001) [3]. The third adsorption structure, $p(2\sqrt{3} \times 2\sqrt{3})R30°$, observed in [3] with very low coverage, was not producible with benzene on Co(0001). This structure was also observed in adsorption studies of benzene on Ni(111) in addition to the $p(\sqrt{7} \times \sqrt{7})R19.1°$ structure [6].

## 5.3 Collection of IV-curves for structure analysis

The $p(\sqrt{7} \times \sqrt{7})R19.1°$ structure was chosen to be analysed in detail, since it corresponds the saturation coverage. Besides, the quality of the pictures taken from this structure was much better that the quality of pictures from the $c(2\sqrt{3} \times 4)rect$ structure, as can be seen from fig. 5.3.

For detailed structure analysis LEED–IV-curves from the observed structure were needed, therefore a complete set of LEED images were recorded from the $p(\sqrt{7} \times \sqrt{7})R19.1°$ structure. In order to achieve best possible contrast and sharpness of the diffraction pattern, LEED–IV-scans were made after dosing 50 L benzene at the temperature of 220 K. With these parameters a sharp diffraction pattern was observed with reasonable stability. The measurements and the data collection were made as explained in section 4.3.3. The energy range measured was 20–500 eV in

2 eV steps. The whole range had to be measured in several parts since the structure eroded during the electron bombardment. Individual parts ranged from 40 to 150 electron volts; the shortest ones are from the low energy side of the range. The temperature during the LEED–IV-measurements was 170 K.

After the measurements the data was analyzed to obtain the IV-curves from the recorded pictures. The intensities of the curves were collected picture by picture. The collection was made with "Ivanal" program, coded in Laboratory of physics. There are several versions of the program and the latest version, modified by M. Aronniemi in 1999 [38] and called "Hydroiv", was used. The intensities of the different beams were collected by integrating the intensities in the vicinity of the spot in question from all pictures recorded. The locations of the spots were defined either visually or, if not possible, due to low intensity, by following the paths created from the locations of the spots in previous pictures.

When intensity curves from all beams in one set of pictures were collected, the intensity versus energy curves of symmetry equivalent beams were averaged. In this case this meant averaging either 6 (for integral) or 12 (for fractional) beams. However, before averaging, the quality of the individual curves were confirmed and the low quality curves, if some, were dismissed. After averaging, the energy scale was calibrated, since the correct energy differed slightly from the recorded one. This calibration had to be done for each set separately, since the offset in energy varied between the sets of pictures.

The intensity of a single beam was collected from several sets of pictures in order to obtain as long energy range as possible. The range was limited above by the rising background, which eventually prevented the particular spots to be distinguished from the pictures, and below by the angle of diffraction, since the spots appeared on the screen not until the angle between the incident and diffracted beam was small enough: the higher the index of the spot, the later it appeared on the screen.

Since the conditions (e.g. the current of the electron beam, suppressing voltage, etc.) varied from measurement to measurement, the IV-curves from different measurements could not be joined together directly. The overlapping parts of the adjacent curves were used in carrying out a reliable joining of the curves. The adjacent curves

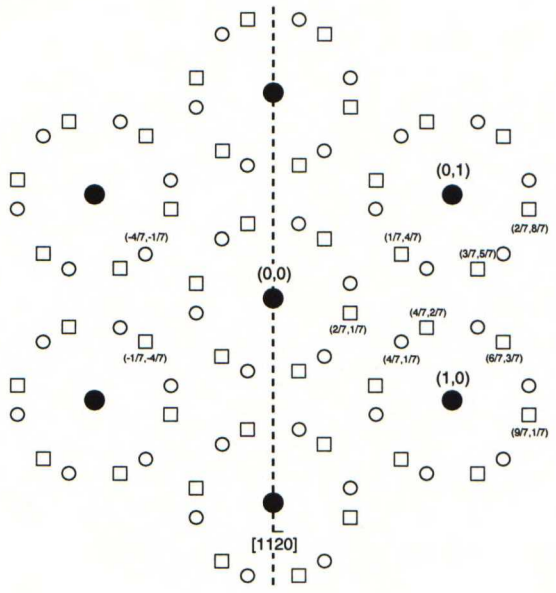


Figure 5.5. *Indexing of the fractional order beams in* $p(\sqrt{7} \times \sqrt{7})R19.1°$ *structure. The first integral order beams are also shown. "•" indicates integral order spots and "○" and "□" indicate different domains of fractional order spots. The indexing is presented for "□" domain for simplicity purposes only. Spot* $(\frac{4}{7}, \frac{1}{7})$ *in domain "□" equals spot* $(\frac{1}{7}, \frac{4}{7})$ *in domain "○" as indexed in text. The dashed line corresponds to mirror axis along* $[11\bar{2}0]$.

were scaled so that the forms of the overlapping parts of the curves were as identical as possible. This was done by comparing the intensities of the curves in the overlapping regions. The comparison yielded to a scaling factor and an offset value. The other curve was then scaled by using newly derived parameters and joined to the other curve. The rest of the short parts were joined together similarly to form a complete IV-curve.

From the observed diffraction pattern it was possible to distinguish total of ten different diffracted beams: 3 integral ((1,0), (1,1) and (2,0)) and 7 fractional ($(\frac{2}{7}, \frac{1}{7})$, $(\frac{4}{7}, \frac{1}{7})$, $(\frac{4}{7}, \frac{2}{7})$, $(\frac{5}{7}, \frac{3}{7})$, $(\frac{6}{7}, \frac{3}{7})$, $(\frac{8}{7}, \frac{2}{7})$, and $(\frac{9}{7}, \frac{1}{7})$) order beams. The IV-curves measured from these beams are presented in figs. B.1 and B.2 in appendix B. The indexing of the measured fractional order beams is presented in fig. 5.5. The first integral order beams are also shown.

Symmetry of the $p(\sqrt{7}\times\sqrt{7})R19.1°$ LEED pattern is high because of the $[11\bar{2}0]$ mirror axis: Hexagonal close packed surfaces generally have 3-fold rotational symmetry, but since there are two non-equivalent terraces (i.e. (0001) and (0002)) which differ by a rotation of 180°, or equivalently 60°, the surface has a 6-fold symmetry rather than 3-fold as would be the the case without the mirror plane.

The averaging of the beams from the different domains may be understood by investigating beams in fig. 5.5: The beam $(\frac{4}{7}, \frac{1}{7})$ belongs to domain "o" and the mirror plane runs along the dashed line between (-1,1) and (1,-1) LEED spots in fig. 5.5. Consequently it is equivalent to $(\frac{-1}{7}, \frac{-4}{7})$ in domain "□", but not to $(\frac{-4}{7}, \frac{-1}{7})$; the latter is equivalent to $(\frac{1}{7}, \frac{4}{7})$. The existence of the non-equivalent terraces (0001) and (0002) causes averaging of the beams rotated 180° with respect to each other. This means that the spots $(\frac{4}{7}, \frac{1}{7})$ and $(\frac{-4}{7}, \frac{-1}{7})$ are averaged so that the both spots in fact are averages of each other and are thus equal. This is valid also for $(\frac{1}{7}, \frac{4}{7})$ and $(\frac{-1}{7}, \frac{-4}{7})$. All four spots are therefore a mixture of same kind of beams, which makes their intensities, and therefore their IV-curves, equal. This mixing applies for all observed LEED spots thus the spots with equal $|k_{||}|$ are equal. In collecting the IV-curves averaging of 6 or 12 different beams with the same $|k_{||}|$ was therefore justified.

## 5.4 Speculative adsorption structures

The analysis of the measured IV-curves was done in Tampere University of Technology by K. Pussi and M. Lindroos [39]. In the analysis multilayer relaxation of benzene covered Co(0001) was studied by tensor–LEED. Three integral ((1,0), (1,1) and (2,0)) and four fractional (($\frac{2}{7}$,$\frac{1}{7}$), ($\frac{4}{7}$,$\frac{1}{7}$), ($\frac{4}{7}$,$\frac{2}{7}$) and ($\frac{5}{7}$,$\frac{3}{7}$)) IV-curves were used in the analysis with a total energy range of 1402 eV. The analysis was done in three steps at 170 K.

Eight possible high symmetry adsorption sites had to be taken into account: two top sites, two fcc sites, two hcp sites and two bridge sites. These sites are shown in fig. 5.6. Similar sites are labeled with A and B according to the orientation of the benzene molecule: A corresponds to sites where parallel C–C bonds of benzene

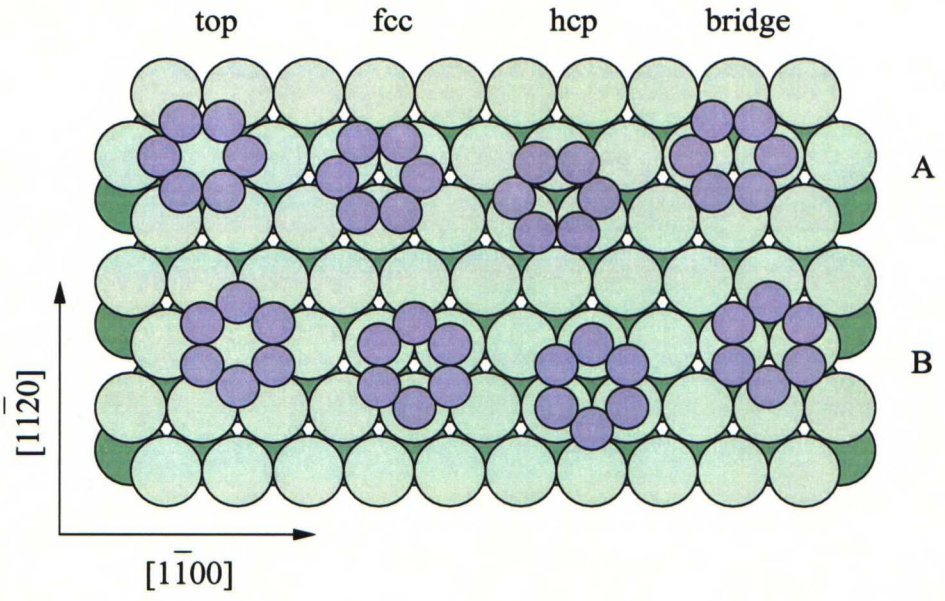


Figure 5.6. *High symmetry adsorption sites of benzene on Co(0001).*

molecules are aligned in [11$\bar{2}$0] direction and B to sites where the parallel bonds are aligned in [1$\bar{1}$00] direction. There is a three-fold rotation axis on top, fcc and hcp sites but not on bridge sites. The substrate has a six-fold symmetry (a three-fold rotation with a symmetry axis). The different symmetry of the substrate and the adsorbate sites leads to averaging of domains explained in section 5.3, which had to be considered in the analysis: All three-fold sites had two domains and the bridge sites six domains to be averaged.

In the first stage of the analysis the screening for the possible structures were made. In the screening process the only parameter varied was the metal-carbon bond length. It was varied from 1.80 Å to 2.40 Å in steps of 0.05 Å. The benzene ring was kept flat on the surface with C–C distance of 1.40 Å. Other parameters used were the imaginary part of the inner potential -5 eV and the Debye temperatures for cobalt 385 K and for carbon 420 K. The resulting Pendry R-factors ($R_P$) are shown in table 5.1.

Table 5.1. *Pendry R-factors for calculated structures. In the first stage the metal-carbon bond was varied, in the second also the relaxation of the benzene molecule and the first Co layer was allowed and in the refinement stage rest of the parameters were released and optimized.*

| Geometry | $R_P$ (stage 1) | $R_P$ (stage 2) | $R_P$ (refinement) |
|---|---|---|---|
| top A | **0.32** | **0.28** | - |
| top B | **0.37** | 0.33 | - |
| fcc A | 0.41 | - | - |
| fcc B | 0.48 | - | - |
| hcp A | **0.34** | **0.30** | **0.28** |
| hcp B | 0.47 | - | - |
| bridge A | **0.33** | 0.33 | - |
| bridge B | 0.47 | - | - |

In the second stage only the sites with $R_P$ within the variance of the the best Pendry R-factor, called RR-factor, were considered. The RR-factor was 0.16, thus the sites with $R_P$=0.37 or under were taken under further consideration. Acceptable factors are marked with bold values in the table, corresponding to top A and B, hcp A and bridge A sites. In the second stage the benzene ring was allowed to relax according to the symmetry of the site in addition to the allowed relaxation of the first cobalt layer.

The Pendry R-factors resulted from the second stage are tabulated also in 5.1. There still was two possible sites, top A and hcp A, only considering the $R_P$-factors. However, after a second R-factor, $R_2$, was taken under consideration, the hcp A site clearly resulted to better fit. The $R_2$-factors for the sites were 0.21 for top A and 0.17 for hcp A structure. The $R_P$-factors weights the positions and the shapes of the peaks whereas $R_2$ gives more weight to intensity ratios of the peaks. The very short cobalt-carbon bond of the top A site, 1.82 Å, also speaks on behalf of the hcp A site, since the bond length this short is in the limit of being chemically reasonable. The sum of the covalent bond length of carbon and metallic radii of cobalt is 1.96 Å, thus the contraction would have been as high as -7 %.

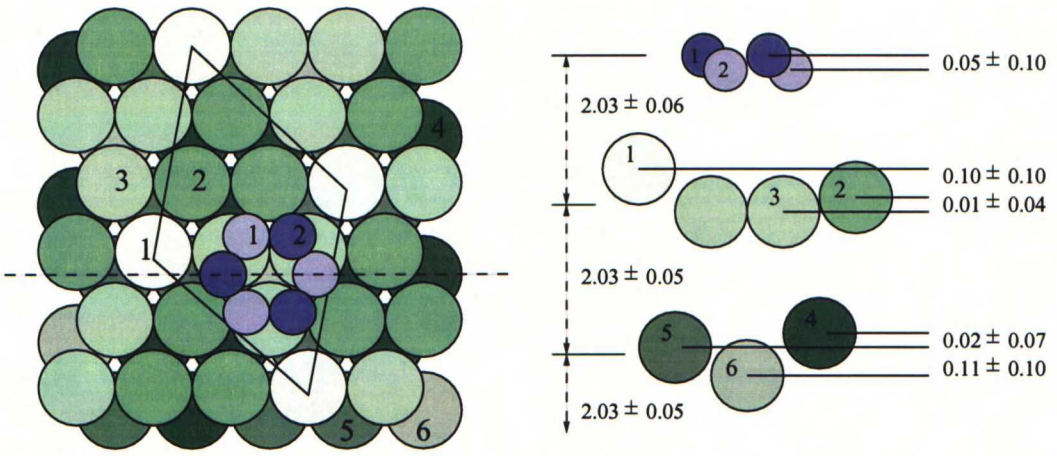


(a) Top view (b) Side view

Figure 5.7. *The favored adsorption structure: a) Top view of the benzene molecule on the hcp A site. The solid line presents a* $p(\sqrt{7} \times \sqrt{7})$ *unit cell. b) Cut along the dashed line (in* $[1\bar{1}00]$ *direction). All parameters shown are in Ångströms.*

The third stage, called refinement, was calculated only for hcp A site. In this stage the second and the third cobalt layers were allowed to relax and the non structural parameters were optimized. These parameters were the imaginary part of the inner potential and the Debye temperatures. In addition a new set of phase shifts were calculated for the favored structure.

The resulting calculated IV-curves for the best fit geometry, hcp A, with the experimental curves, are presented in fig. 5.8 (integral order curves) and in fig. 5.9 (fractional order curves). $R_P$-factors for each curve are also included to the figures. The total Pendry R-factor was $R_P$=0.28.

### 5.4.1 Structural parameters

As a result of the IV-analysis, the benzene molecule was found to adsorb on a hcp A site. The geometrical parameters resulted are presented in table 5.3 with errors for z values estimated by the RR-factor. The origin is chosen to be in the middle of the

benzene ring.

The resulting structure is drawn in fig. 5.7. In fig. 5.7(a) the unit cell with symmetry equivalent atoms is shown and in fig. 5.7(b) there is a cut along the dashed line in fig. 5.7(a) in $[1\bar{1}00]$ direction showing some of the structural parameters. The C–C bond length of the benzene molecule was 1.40 Å, and the buckling of the benzene ring $0.05 \pm 0.10$ Å. The average distance between the molecule and the first cobalt layer was $2.03 \pm 0.06$ Å and the shortest Co–C bond $2.15 \pm 0.06$ Å. The interlayer spacing between the first and the second cobalt layer was $2.03 \pm 0.05$ Å and between the second and the third cobalt layer $2.03 \pm 0.05$ Å as can be seen from fig. 5.7(b). The first and the second cobalt layers were also strongly buckled: The first by 0.11 Å and the second by 0.13 Å.

### 5.4.2 Discussion

Comparing the resulted parameters with the previously calculated values for clean Co(0001) [40], the distance between first and the second cobalt layer expands 0.04 Å (+2.0 %) and the distance between the second and the third layer contracts 0.03 Å (-1.5 %). Interlayer distances thus equal the bulk value of 2.03 Å.

Recently W. Braun et al. [3] studied benzene adsorption on Ru(0001). As a result they concluded that the benzene adsorbs on hcp A site and the C–C bond length of the benzene molecule slightly expands (expansion under 0.01 Å) but still remain compatible with the gas phase value of 1.40 Å. They also concluded that buckling of the benzene ring was 0.08 Å, and the shortest metal-carbon bond length 2.11 Å. The average distance between the benzene molecule and the first substrate layer was 2.09 Å. Interlayer distances in ruthenium chanced so that the first is contracted by -4 % and the second expanded by 1 %. The relaxations of the layers were thus to opposite directions to the relaxations found in this work. The Pendry R-factor in [3] was 0.28.

G. Held et al. [8] studied the adsorption of benzene on Ni(111) and they also found that the benzene adsorbs on hcp A site with slightly expanded C–C bonds of 1.48 Å and 1.50 Å. The buckling of the benzene molecule was found to be 0.04 Å and the

Table 5.2. *Adsorption geometries of benzene on various metal surfaces.* $d_C - C$ *is the C–C bond length of the benzene ring on the surface. Two values indicate ring distortion with short and long bonds. The gas phase value of the C–C bond is 1.395 Å.* $d_{C-M}$ *is the average benzene-metal distance.*

| Substrate | a (Å) | Site | $d_{C-C}$ (Å) | $d_{C-M}$ (Å) | $R_P$ | Ref. |
|---|---|---|---|---|---|---|
| Ni(111) | 2.49 | hcp A | 1.43/1.55 | 1.91 | 0.26 | [8] |
| | | hcp A | 1.40/1.46 | 1.91 | 0.28 | [9] |
| Co(0001) | 2.51 | hcp A | 1.40 | 2.03 | 0.28 | This work |
| Rh(111) | 2.68 | hcp A | 1.46/1.58 | 2.20 | 0.41 | [11]† |
| | | hcp A | 1.37/1.50 | 2.19 | 0.22 | [12]† |
| Ru(0001) | 2.71 | hcp A | 1.45/1.48 | 2.09 | 0.28 | [3] |
| Pd(111) | 2.75 | fcc A | 1.40/1.46 | 2.30 | 0.22 | [12]† |
| | | fcc A | 1.40/1.46 | 2.25 | 0.48 | [41]† |

† Benzene coadsorbed with CO.

average distance between the molecule and the substrate 1.91 Å. The nickel layers were relaxed by +0.08 Å (first) and -0.06 Å (third). The Pendry R-factor was 0.26.

These and more LEED-IV based results on benzene on various transition metal surfaces are presented in table 5.2. The values on Rh(111) and Pd(111), however, are from benzene coadsorbed with CO and this has to be taken into account when comparing the values.

Table 5.3. *Geometrical parameters for the favored structure, with error bars calculated with the help of the RR-factor in z direction. The origin is chosen to be in the middle of the benzene ring. The indexing of the atoms is shown in fig. 5.7.*

| Atom | x (Å) | y (Å) | z (Å) | Δz (Å) |
|---|---|---|---|---|
| $C_1$ | -1.40 | 0.00 | 0.00 | ±0.09 |
| $C_1$ | 0.70 | 1.20 | 0.00 | ±0.09 |
| $C_1$ | 0.70 | -1.20 | 0.00 | ±0.09 |
| $C_2$ | 1.40 | 0.00 | 0.05 | ±0.10 |
| $C_2$ | -0.70 | 1.20 | 0.05 | ±0.10 |
| $C_2$ | 0.70 | -1.20 | 0.05 | ±0.10 |
| $Co_1$ | 2.51 | 2.89 | 1.91 | ±0.15 |
| $Co_2$ | 1.25 | 0.72 | 2.07 | ±0.06 |
| $Co_2$ | 5.01 | 2.89 | 2.07 | ±0.06 |
| $Co_2$ | 1.25 | 5.02 | 2.07 | ±0.06 |
| $Co_3$ | 5.01 | -1.45 | 2.08 | ±0.03 |
| $Co_3$ | 2.51 | -1.45 | 2.08 | ±0.03 |
| $Co_3$ | 3.76 | 0.72 | 2.08 | ±0.03 |
| $Co_4$ | 3.76 | -2.17 | 4.05 | ±0.07 |
| $Co_4$ | 5.01 | 0.00 | 4.05 | ±0.07 |
| $Co_4$ | 2.51 | 0.00 | 4.05 | ±0.07 |
| $Co_5$ | 3.76 | 2.17 | 4.07 | ±0.07 |
| $Co_5$ | 1.25 | 2.17 | 4.07 | ±0.07 |
| $Co_5$ | 2.51 | 4.34 | 4.07 | ±0.07 |
| $Co_6$ | 5.01 | -4.34 | 4.18 | ±0.15 |

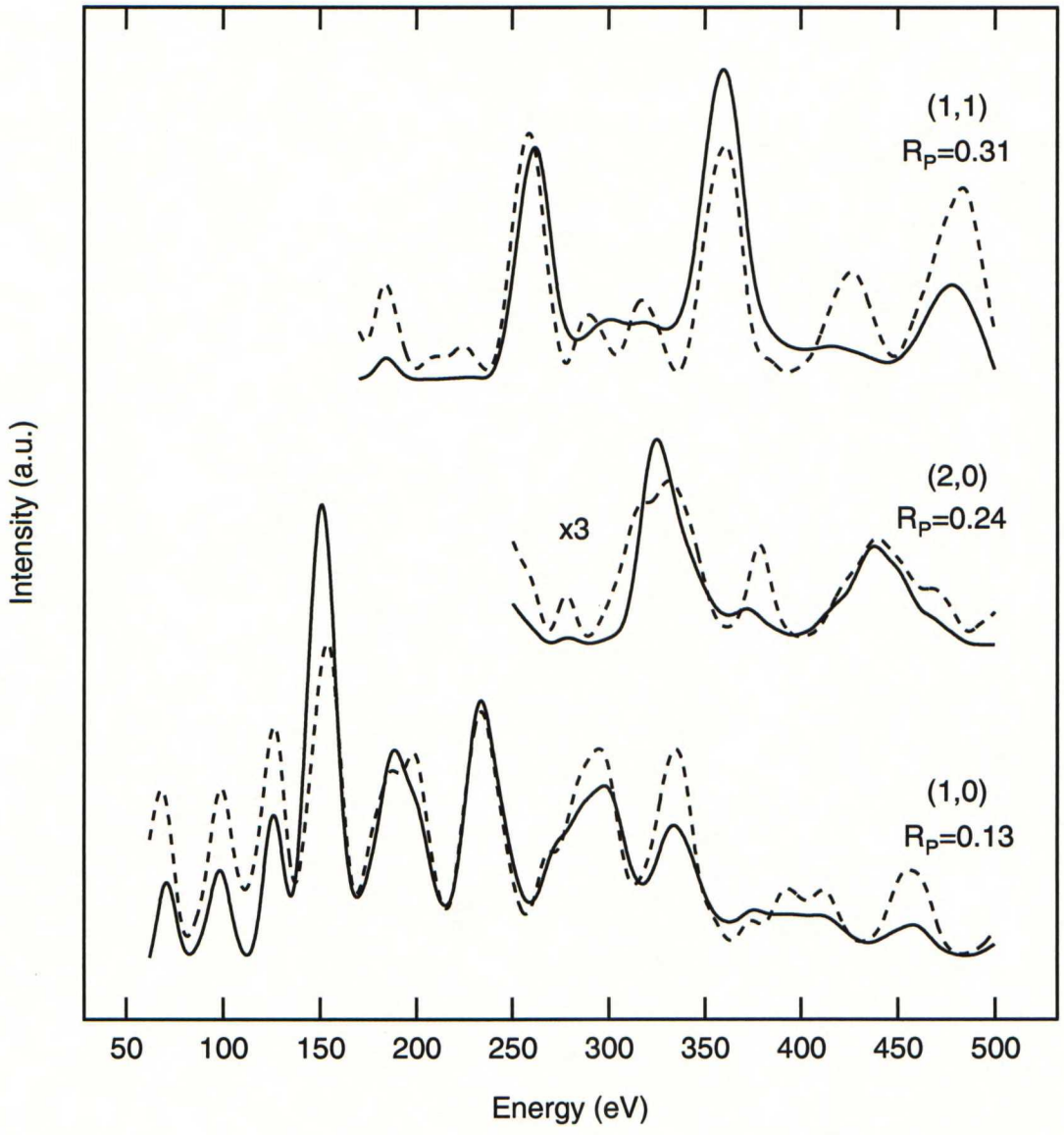


Figure 5.8. *Experimental (solid) and calculated (dashed) IV-curves of the fractional order spots for the best fit geometry of the* $p(\sqrt{7} \times \sqrt{7})R19.1°$ *structure. Corresponding* $R_P$*-factors are also included. The total Pendry R-factor for the best fit geometry was* $R_P$*=0.28.*

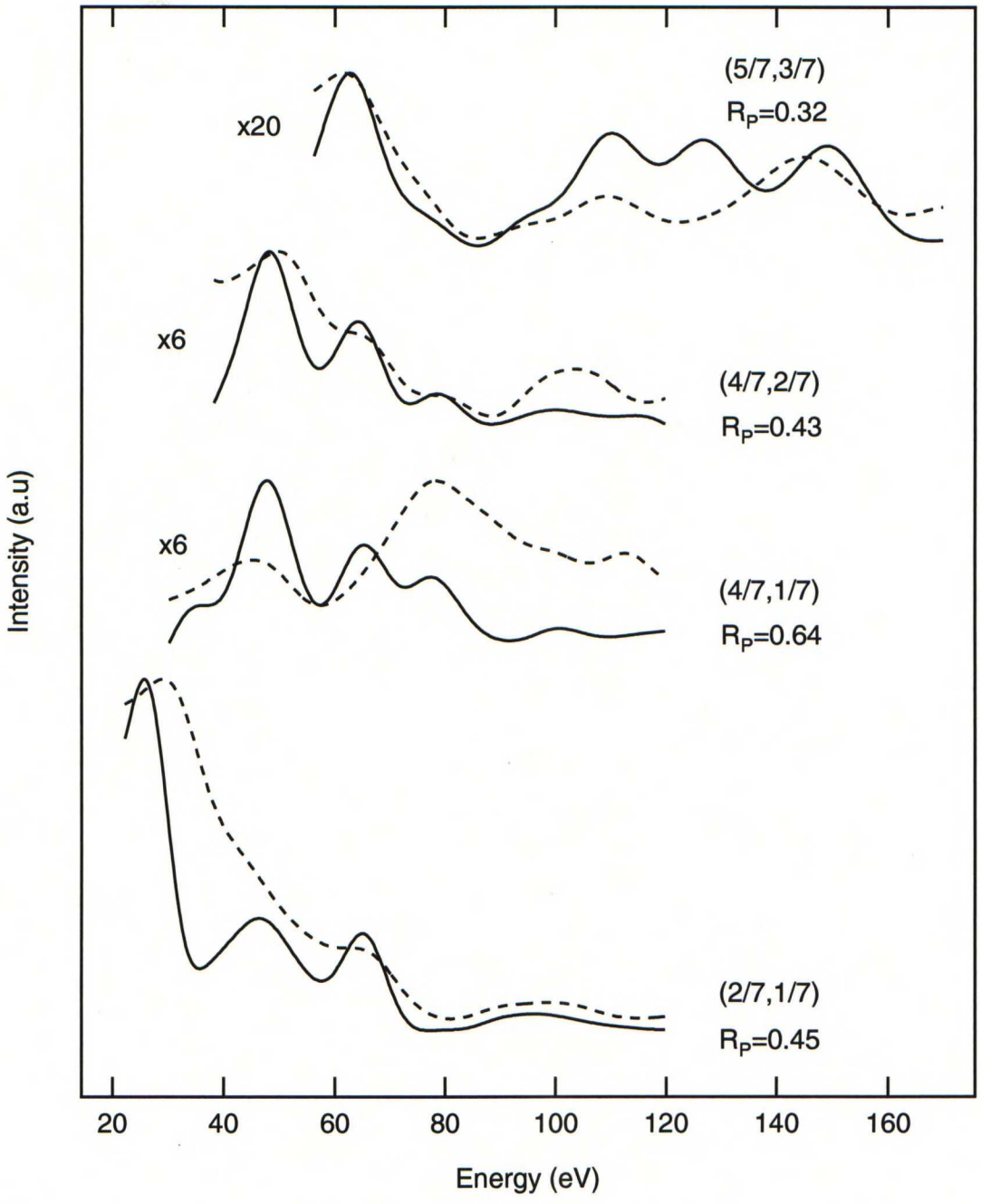


Figure 5.9. *Experimental (solid) and calculated (dashed) IV-curves of the fractional order spots for the best fit geometry of the* $p(\sqrt{7} \times \sqrt{7})R19.1°$ *structure. Corresponding* $R_P$*-factors are also included. The total Pendry R-factor for the best fit geometry was* $R_P$*=0.28.*

# Chapter 6

# Conclusions

In this work the adsorption of benzene on Co(0001) has been studied by LEED–IV. The study started with the determination of the adsorption phases of benzene and continued by the measurements of the LEED–IV-curves from the saturated structure. The measured curves were then used to determine the adsorption geometry of benzene by LEED–IV-analysis.

The Benzene adsorbs molecularly on Co(0001) at room temperature and below. Adsorbed benzene partly dehydrogenates around 340 K forming some hydrocarbon intermediate, most likely $C_6H_5$. The intermediate stays on the surface during heating. The activation energy of the decomposition is around 102 kJ/mole. The adsorption of benzene also induces a work function change of -1.3 eV corresponding to an initial dipole moment of 1.9 Debye/mole.

Benzene was found to form two adsorption phases: A $c(2\sqrt{3} \times 4)rect$ superstructure at room temperature with all coverages and below room temperature with low coverages. This structure corresponds to benzene coverage $\theta_{ideal} = 0.125$ or carbon coverage $\theta_C = 0.75$. Below room temperature and with higher coverages benzene forms a $p(\sqrt{7} \times \sqrt{7})R19.1°$ superstructure corresponding to saturated benzene. The coverage of benzene for this structure is $\theta_{ideal} = 0.143$ or $\theta_C = 0.858$ for carbon. The $p(\sqrt{7} \times \sqrt{7})R19.1°$ structure was detected over a wide range of doses and temperatures.

From the saturated $p(\sqrt{7} \times \sqrt{7})R19.1°$ structure LEED–IV-curves were recorded resulting to three integral order beams and seven fractional order beams. The curves were recorded with the energies between 20 and 500 electronvolts resulting in the total energy range of 1640 eV.

Three integral and four fractional order beams with an energy range of 1402 eV were used in the LEED–IV. As a result of the analysis, benzene molecules were found to be adsorbed on hcp sites parallel C–C bonds aligned in $[1\bar{1}00]$ direction. The length of the C–C bonds equaled the gas phase value of 1.40 Å. The benzene ring was buckled by $0.05 \pm 0.10$ Å. The distance of the molecule from the surface was $2.03 \pm 0.06$ Å and the shortest cobalt-carbon distance was $2.15 \pm 0.05$ Å.

Adsorption of benzene also induced substrate relaxations. The distance of the two topmost layers was found to increase to $2.03 \pm 0.05$ Å, corresponding to an expansion by 2.0 %. The distance between the second and the third layer was on the contrary decreased to $2.03 \pm 0.05$ Å, corresponding to a contraction of -1.5 %. The cobalt layers were also strongly buckled: the first by 0.11 Å and the second by 0.13 Å.

Since the recording of the IV-curves from the $c(2\sqrt{3} \times 4)rect$ structure was not possible during this work, the apparent continuation would be the detailed analysis of the rectangular structure. Also the already measured $p(\sqrt{7} \times \sqrt{7})R19.1°$ IV-curves would need a little refinement since there might be some inaccuracy in the intensities of the IV-curves caused by the joining of the partial curves. The amount of the fractional beams used in analysis could also be increased.

# Bibliography


[1] P. Jakob and D. Menzel, Surf. Sci. **201**, 503 (1988).

[2] C. Stellwag, G. Held, and D. Menzel, Surf. Sci. **325**, L379 (1995).

[3] E. Braun *et al.*, Surf. Sci. **475**, 18 (2001).

[4] M. Stichler, R. Weimar, and D. Mezel, Surf. Sci. **384**, 179 (1997).

[5] W. Huber, H.-P. Steinrück, T. Pache, and D. Menzel, Surf. Sci. **217**, 103 (1989).

[6] H.-P. Steinrück, W. Huber, T. Pache, and D. Menzel, Surf. Sci. **218**, 293 (1989).

[7] W. Huber, P. Zebisch, T. Bornemann, and H.-P. Steinrück, Surf. Sci. **258**, 16 (1991).

[8] G. Held, M. Bessent, S. Titmuss, and D. King, J. Chem. Phys **105**, 11305 (1996).

[9] O. Schaff *et al.*, Surf. Sci. **348**, 89 (1996).

[10] B. Koel, J. Crowell, C. Mate, and G. Somorjai, J. Phys. Chem **88**, 1988 (1994).

[11] R. Lin, G. Blackmann, M. V. Hove, and G. Somorjai, Acta Chryst. **B 43**, 368 (1987).

[12] A. Barbieri, M. V. Hove, and G. Somorjai, Surf. Sci. **306**, 261 (1994).

[13] D. Ogletree, M. V. Hove, and G. Somorjai, Surf. Sci. **183**, 1 (1987).

[14] A. Wander *et al.*, Surf. Sci. **249**, 21 (1991).

[15] K. Habermehl-Ćwirzeń, J. Katainen, J. Lahtinen, and P. Hautojärvi, Surf. Sci. (2002), in print.

[16] H. Lüth, *Surfaces and Interfaces of Solid Materials*, 3rd ed. (Springer, New York, 1997).

[17] J. Thomas and W. Thomas, *Introduction to the heterogeneous Catalysis* (Academic press, New York, 1967).

[18] D. Hayword and B. Trapnell, *Chemisorption* (Butterwoths, London, 1964).

[19] M. Seah and W. Dech, Surf. Interface Anal **1**, 2 (1979).

[20] K. Christmann, G. Ertl, and O. Shober, Surf. Sci. **40**, 61 (1973).

[21] F. J. Blatt, *Modern Physics* (McGraw-hill, Singapore, 1992).

[22] *Handbook of X-ray Photoelectron Spectroscopy*, edited by J. Moulder, W. Stickle, P. Sobol, and K. Bomben (Perkin-Elmer, Eden Prairie, 1992).

[23] T. Vaara, Ph.D. thesis, Helsinki university of technology, Laboratory of physics, 1997.

[24] H. Ibach and H. Lüth, *Solid-State Physics*, 2nd ed. (Springer, New York, 1997).

[25] J. Lahtinen *et al.*, Surf. Sci. **425**, 90 (1999).

[26] *CRC Handbook of Chemistry and Physics*, 67th ed., edited by R. Weast, M. Astle, and W. Beyer (CRC Press Inc, Boca Raton, 1987).

[27] J. Cland and G. Somorjai, Surf. Sci. **38**, 157 (1973).

[28] S. Minkkinen, Special assingment: LEED-laitteiston automatisointi ja diffraktiokuvien tallennus digitaalisessa muodossa, 1995.

[29] K. Habermehl-Ćwirzeń, K. Kauraala, J. Lahtinen, and P. Hautojärvi, to be published.

[30] H. Graen *et al.*, Surf. Sci. **223**, 33 (1989).

[31] K. Pussi, M. Lindros, and C. Barnes, Chem Phys. Lett. **241**, 7 (2001).

[32] C. Barnes, M. Valden, and M. Pressa, Surf. Rev. Lett. **7**, 67 (2000).

[33] T. Vaara, J. Vaari, and J. Lahtinen, Surf. Sci. **395**, 88 (1998).

[34] J. Lahtinen, J. Vaari, and K. kauraala, Surf. Sci. **418**, 502 (1998).

[35] M. Lindroos, H. Pfnür, P. Feulner, and D. Menzel, Surf. Sci. **180**, 237 (1987).

[36] P. Feulner and D. Menzel, Surf. Sci. **154**, 465 (1985).

[37] S. Lehwald, H. Ibach, and J. Demuth, Surf. Sci. **78**, 577 (1978).

[38] M. Aronniemi, Special assingment: Coverage calibration of hydrogen on Co(0001) surface, 1999.

[39] K. Pussi, report on LEED–IV-analysis: Co{0001}–($\sqrt{7} \times \sqrt{7}$)–$C_6H_6$ (unpublished).

[40] K. Kauraala, Licentiate's thesis, 2000.

[41] H. Ohtami, M. V. Hove, and G. Somorjai, J. Phys. Chem. **92**, 3974 (1988).

[42] J. Katainen, Special assingment: Adsorption of pentane on Co(0001), 2001.

[43] T. Wittrig, P. Szuromi, and W. Weinberg, J. Chem. Phys. **76**, 3305 (1982).

[44] I. Jantunen, Special assingment: Mittausjärjestelyn rakentaminen fotoelektronidiffraktiomittauksia varten, 1999.

[45] J. Sainio, Master's thesis, Helsinki university of technology, Laboratory of physics, 2001.

# Appendix A

# Design and testing of low temperature sample holders

The lowest attainable temperature during surface studies with the current equipment in the Laboratory of physics is 160 K. However, during the latest studies of hydrocarbon adsorption on Co we have faced the need of lower temperatures since for example the desorption temperature of pentane on Co(0001) is below 200 K [42] and studies with other hydrocarbons [43] suggest that the desorption temperature of smaller hydrocarbons on transition metal surfaces is even lower.

In order to enable adsorption studies at a lower temperature, new sample holders were designed. We already had a two stage Varian HV–4 cryostat. It was sufficient to design the sample holders and other parts needed. Design was done so that previously built computer controlled rotatable flange [44] could be mounted into the system.

The work was started by J. Sainio [45], and was finished during this work. J. Sainio considered the problems with heat conduction and heating of the sample together with the need for electrical insulation. He concluded that the electrical insulation is possible to achieve using a sapphire crystal, which is a good thermal conductor at room temperature and electrically insulating. What is more, sapphire has a thermal conductivity that depends on the temperature. Its thermal conductivity is highest at room temperature and decreases rapidly when heated or cooled. This behavior helps

the heating of the sample and allows the sample to be heated with a simple glow bulb. The drawback of the crystal is the lowered heat conduction at low temperatures which limits the achievable temperature range from below. J. Sainio designed also the sample holder for the main chamber [45].

## A.1 Main chamber

The main techniques used in the main chamber, XPS, TDS and LEED, specified the main requirements for the sample cooling system. In addition to cooling, the sample had to be able to be heated and biased to $\pm 100$ V. The LEED-IV-measurements also needed the possibility to rotate the sample around its axis.

As mentioned earlier, these requirements were considered by J. Sainio [45] and the sample holder designed by him is shown in fig. A.7. The holder consists of 5 parts shown in figs. A.8–A.11 in their final form. During the machining of the parts, small changes were made to the original drawings (refer to [45] for original design).

In addition to these parts the system needed an extension rod to attach the holder assembly to the second stage of the cryostat and a radiation shield to reduce the heat radiation to cause additional load on the cryocooler. The radiation shield also helps the heating of the sample since it prevents power loss during heating of the sample. During the design of these parts, the mounting of the system was also considered. The blueprints of the extension rod and the radiation shield are in figs. A.5 and A.6.

Since the computer controlled rotatable flange did not fit directly on top of the chamber, one additional extension tube had to be used below the flange. Above the flange branching for the needed electrical and mechanical feedthroughs had to be added. The whole assembly is shown in fig. A.1.

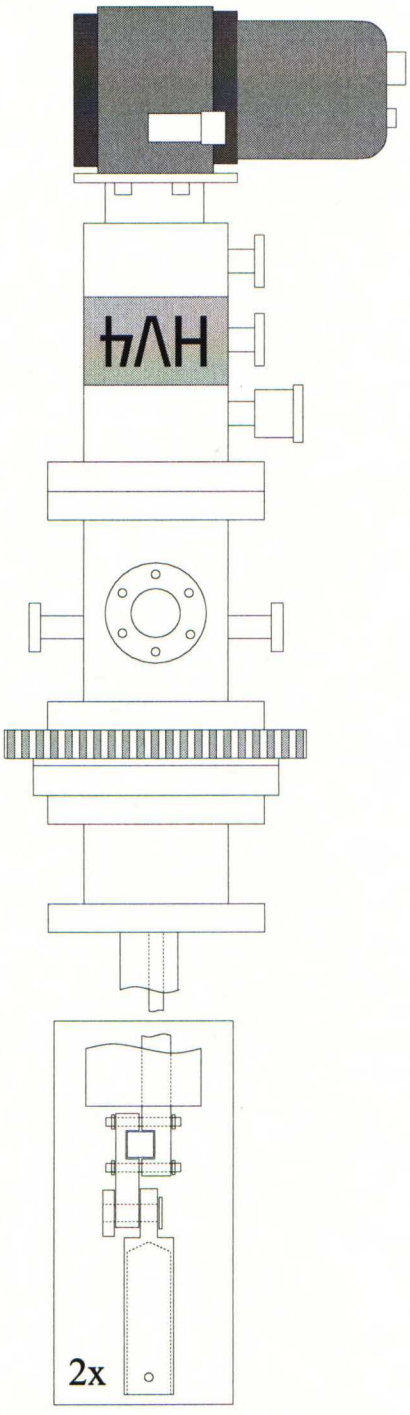


Figure A.1. *The system assembly for the main chamber.*

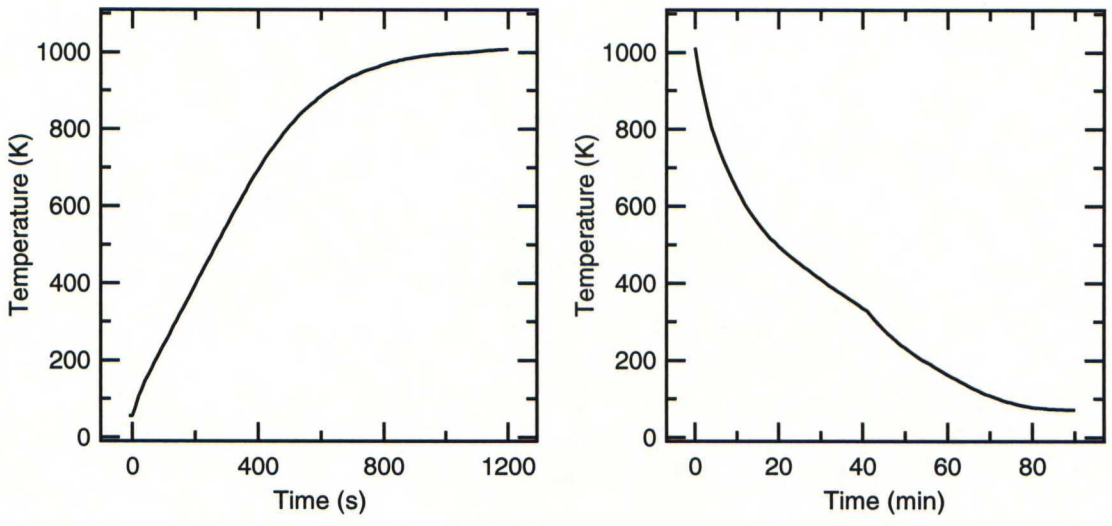


(a) Heating

(b) Cooling

Figure A.2. *System performance of the main chamber.*

### A.1.1 Performance

The testing of the system was made in a small test chamber pumped with a turbomolecular pump. After turning on, cooling of the warm cryocooler took several hours. This initial cooling time, however, is not really of interest, since during the measurements the cryostat is continuously on and higher temperatures (e.g. room temperature) are achieved by heating the sample with an external power supply. During the heating of the sample the temperature of the cryostat itself is quite constant and only the lowest parts of the sample holder are heated significantly. This allows the final temperature of the sample, roughly 70 K, to be achieved in a reasonable time after for example annealing.

Since the time needed to cool down the sample significantly affects the amount of impurities adsorbed on the surface of the sample, an annealing and successive cooling test was made. This test models normal temperature behavior during cleaning procedure of metal samples.

After the cryostat had been cold at least 24 hour the sample was annealed above 1000 K for an hour. The temperature of the sample was recorded during both heating of the sample to the annealing temperature and cooling of it after annealing. The temperature versus time graphs of these parts of the test are illustrated in fig. A.2.

In the fig. A.2(a) there is shown the temperature of the sample during heating the sample holder with a glow bulb inside the holder. The heating voltage was 12.2 V, which led to a heating rate of about 1.6 K/s. This is appropriate heating rate also for TDS measurements and the rate can be adjusted by increasing or decreasing the heating power. Unfortunately, in the beginning of the curve there is a nonlinear region until 150 K is reached with initial heating rate of 2.5 K/s. Thus it may be necessary to use some computer controlled power source in order to achieve a linear temperature ramp during the TDS measurements.

In the fig. A.2(b) there is shown the temperature of the sample after annealing. As can be seen from the graph, the temperature decrease is quite steady until 100 K is reached in 70-80 minutes. In 90 minutes the sample has achieved its final temperature around 70 K. One and a half hours is short enough time to maintain the cleanness of the sample in modern UHV chambers (base pressure under $1 \times 10^{-9}$ Torr).

Mechanical vibrations caused by the cryostat may be a problem during some (e.g. LEED) measurements. Turning off the cooling during these measurements is thus necessary and that causes temperature rise of the sample. However the temperature rise of the sample in one hour is below 30 K, enabling the turning off the cryostat after the final temperature has been achieved and still maintain a low temperature for the time needed for the measurement. There is however some time limit after which the sample starts to warm significantly,hence it limits the time in use for the measurements, which cannot tolerate vibrations.

## A.2 Small chamber

Since the geometry of the small chamber is quite unlike the geometry in the main chamber, totally different sample holder had to be designed. The design of this

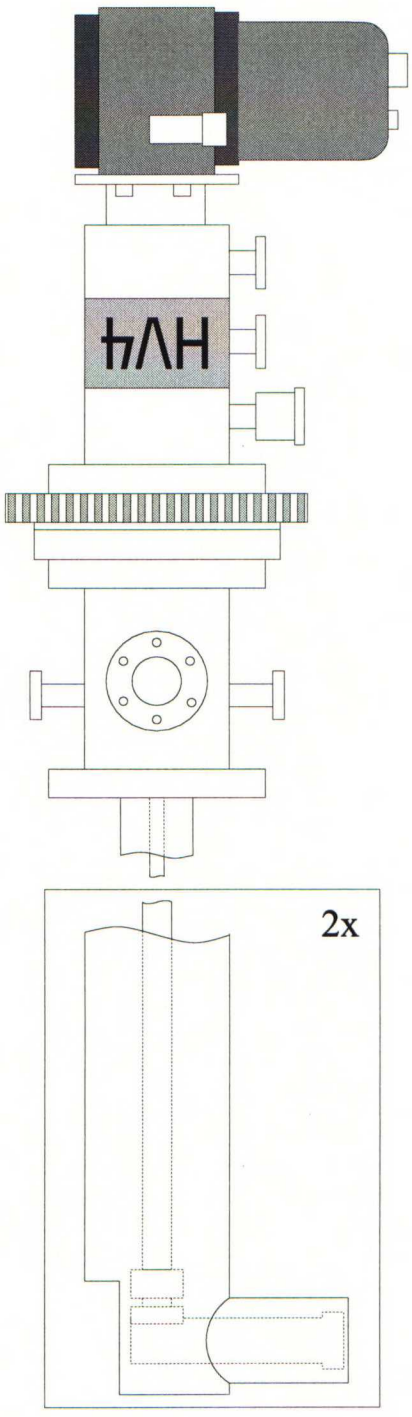


Figure A.3. *The system assembly for the small chamber.*

sample holder was much easier, since the sample did not need to be rotatable around its axis. This led to a design where the holder consists of one piece only. The electrical insulation was again done with the sapphire crystal and the heating with a glow bulb inside the holder.

The design of the holder is shown in fig. A.12. It was machined from one piece of copper since the potential soldering materials cannot tolerate temperatures needed during annealing. The sapphire crystal is mounted between the holder and the extension rod (fig. A.13). The holder is attached to the rod by screws insulated with alumina spacers. A radiation shield was also designed (fig. A.14).

Mounting the system to the small chamber was also easier, since only branching were needed in addition to the rotatable flange. The branching however have to be mounted below the flange in order to enable the rotating of the system. The system assembly for the small chamber is presented in fig. A.3.

### A.2.1 Performance

Similar test, like the ones done with the main chamber system, were also made with this system. The performance examples are presented in fig. A.4. The heating voltage during annealing test (on the left side) was 14,9 V and it induced a heating rate of 2.6 K/s. Unfortunately there is also a nonlinear region in the beginning of the heating, up to 180 K, with initial heating rate of 4.9 K/s.

The temperature behavior during cooling is shown in the fig. A.4(b). The behavior is almost exponential and 100 K is achieved after approximately 70 minutes. The final temperature around 50 K is attained after 80 min cooling.

As a conclusion, both sample holders and constructed systems are suitable for low temperature adsorption studies. They both have their own imperfections, thus it may be convenient to use the old sample holders if higher temperatures are sufficient.

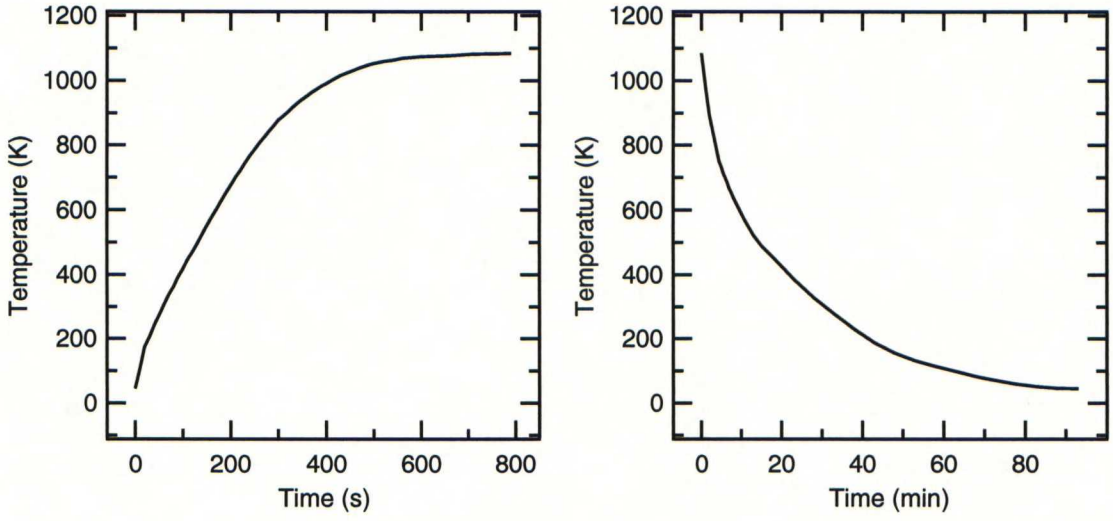


(a) Heating

(b) Cooling

Figure A.4. *System performance of the small chamber.*

# A.3 Blueprints

## A.3.1 Main chamber

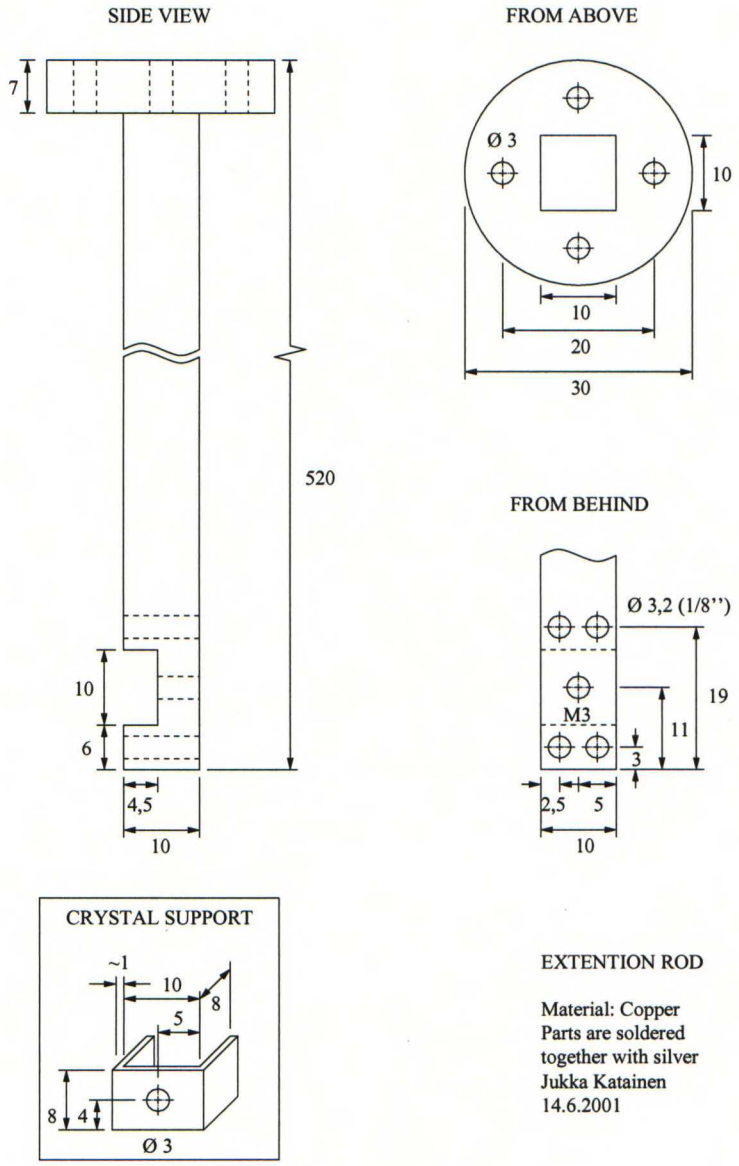


Figure A.5. *Extension rod.*

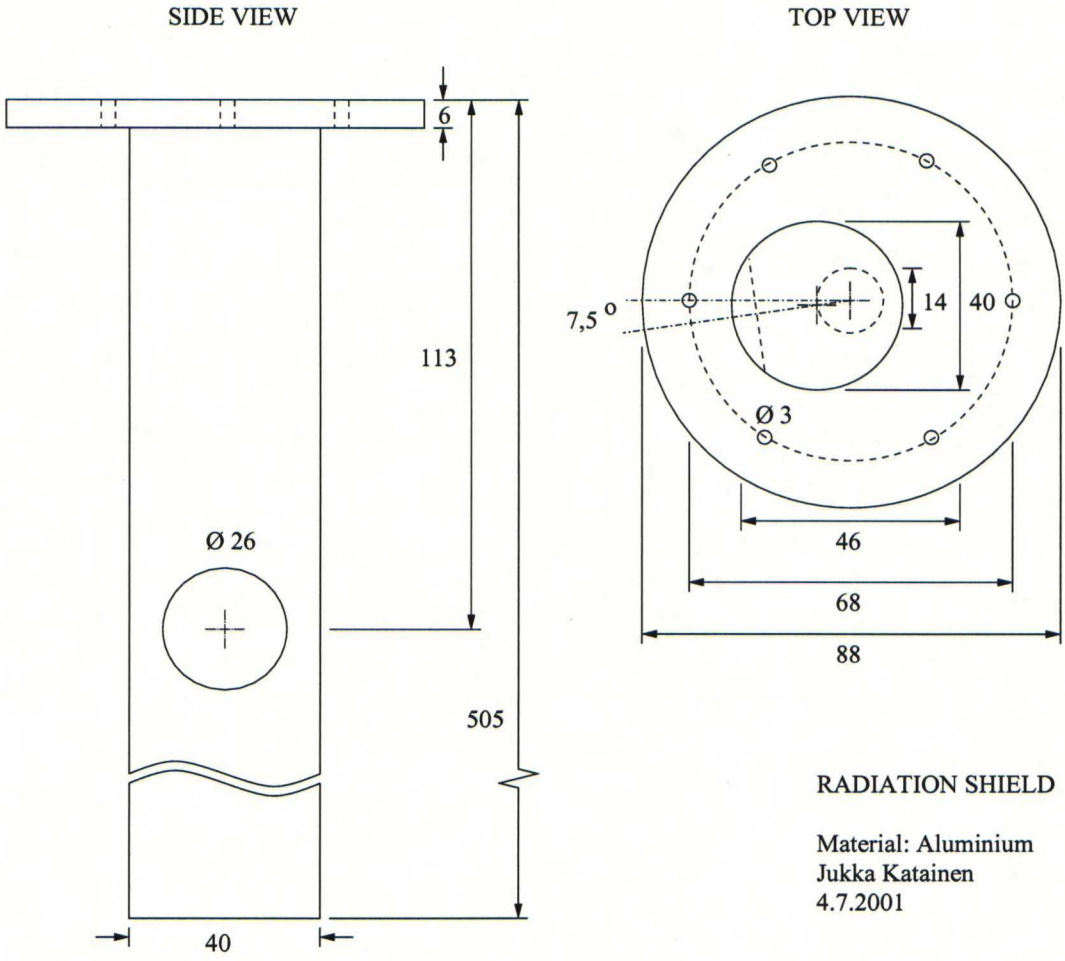


Figure A.6. *Radiation shield.*

### A.3.1.1 Sample holder parts designed by Jani Sainio [45]

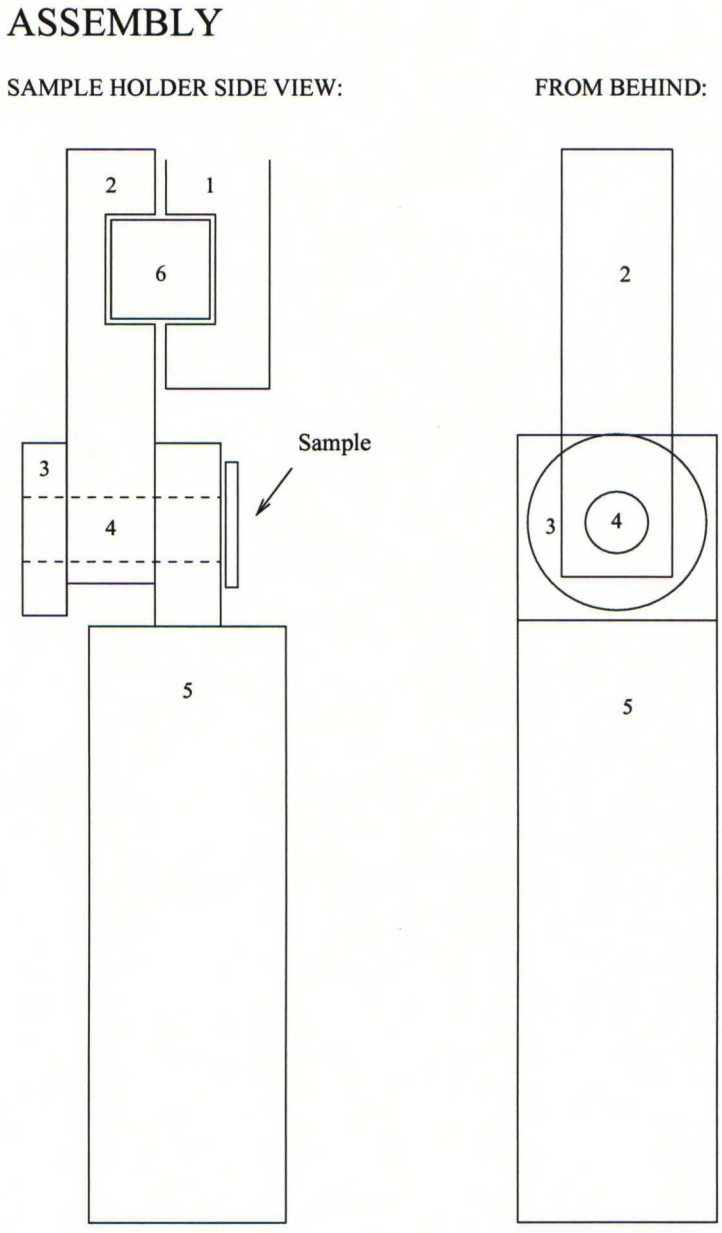


Figure A.7. *Part assembly.*

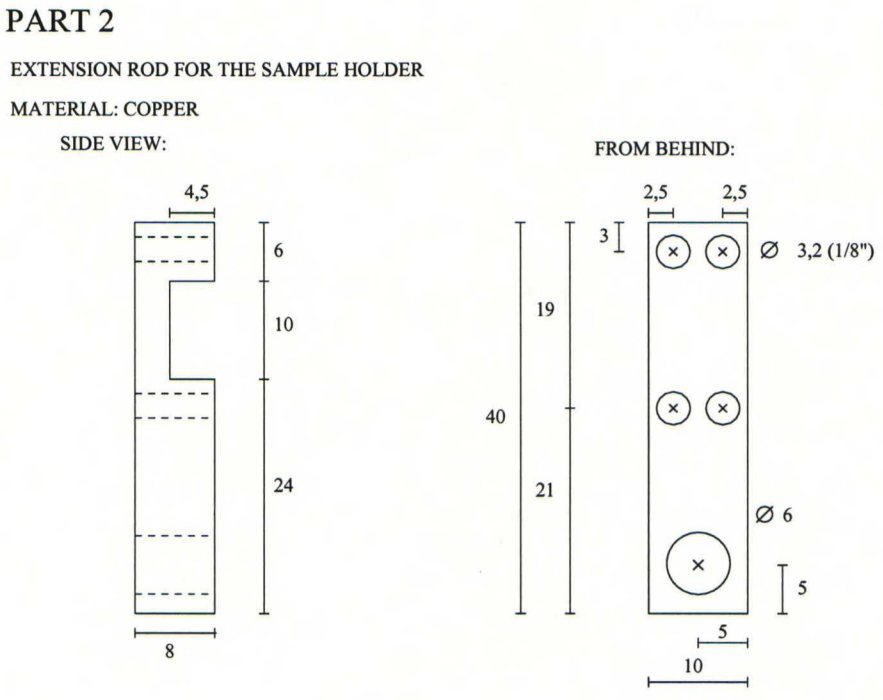


Figure A.8. *Part 2.*




Figure A.9. *Part 4.*

# PART 3

ROTATION DISC 2 PCS
MATERIAL: STAINLESS STEEL

FRONT VIEW:

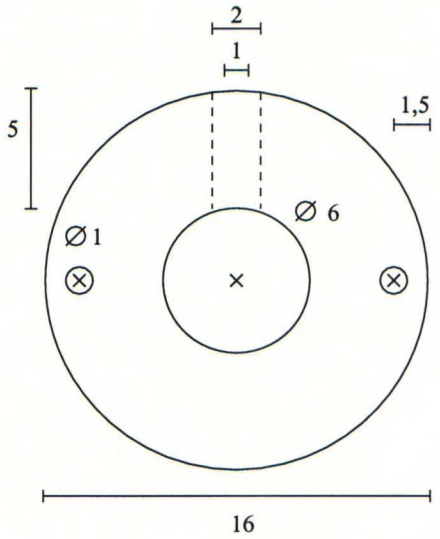


TOP VIEW:

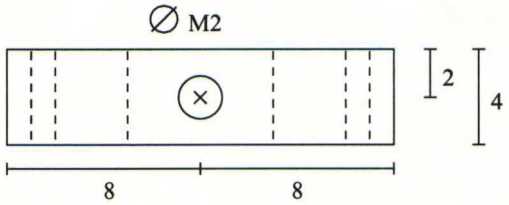


Figure A.10. *Part 3.*

# PART 5

ROTATABLE PART OF THE SAMPLE HOLDER
MATERIAL: COPPER

SIDE VIEW:

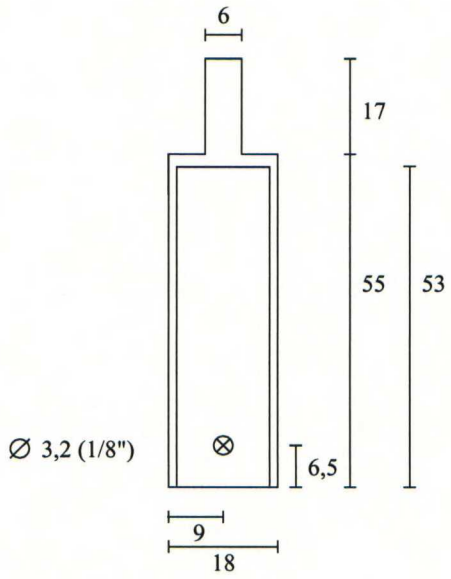


FROM ABOVE:

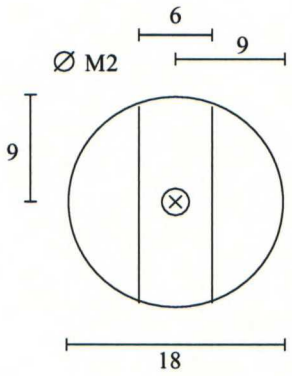


FROM BELOW:

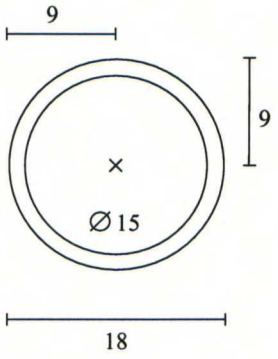


FRONT VIEW:

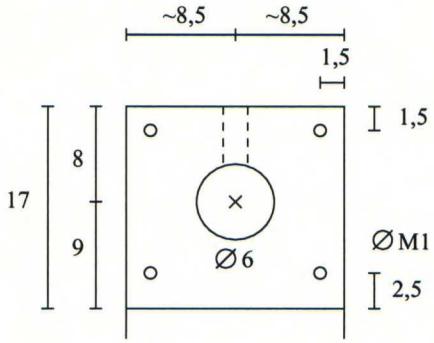


Figure A.11. *Part 5.*

## A.3.2 Small chamber

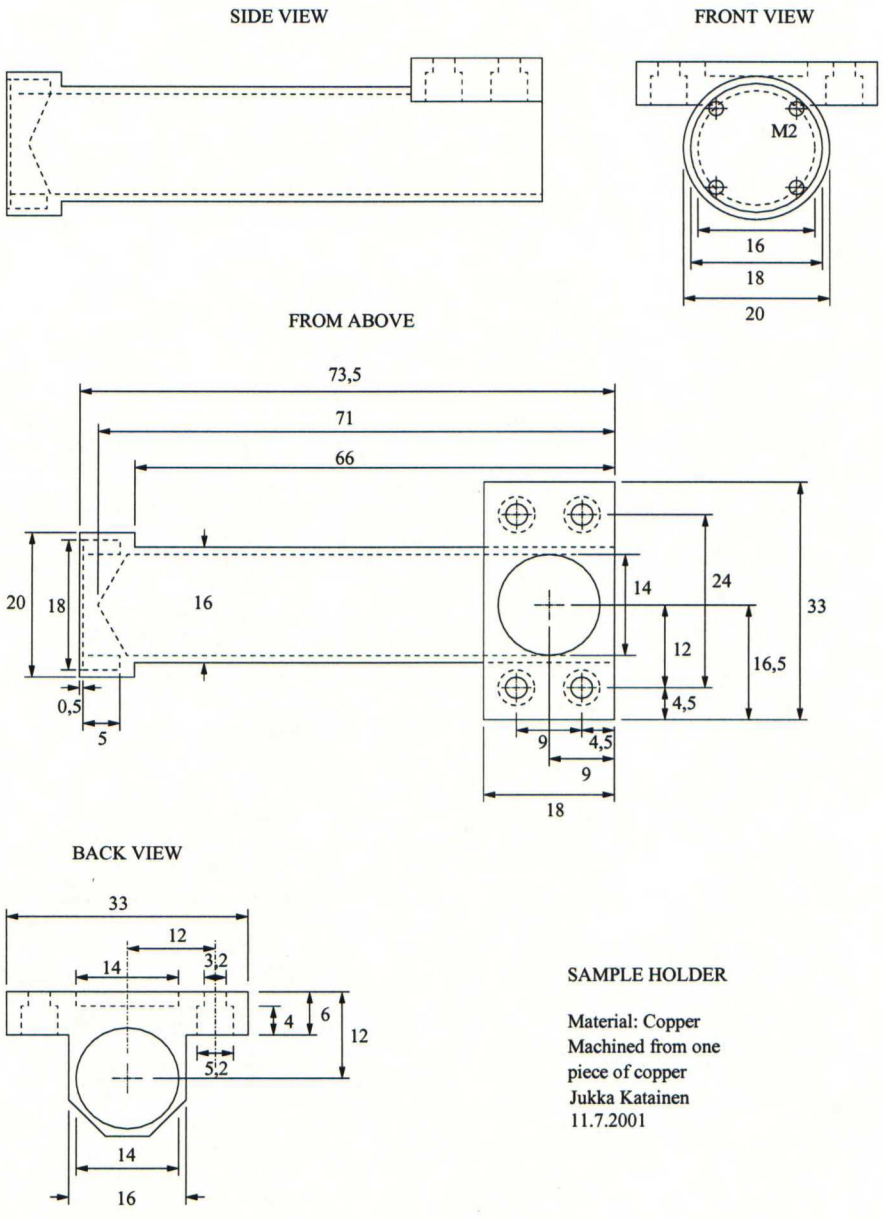


Figure A.12. *Sample holder.*

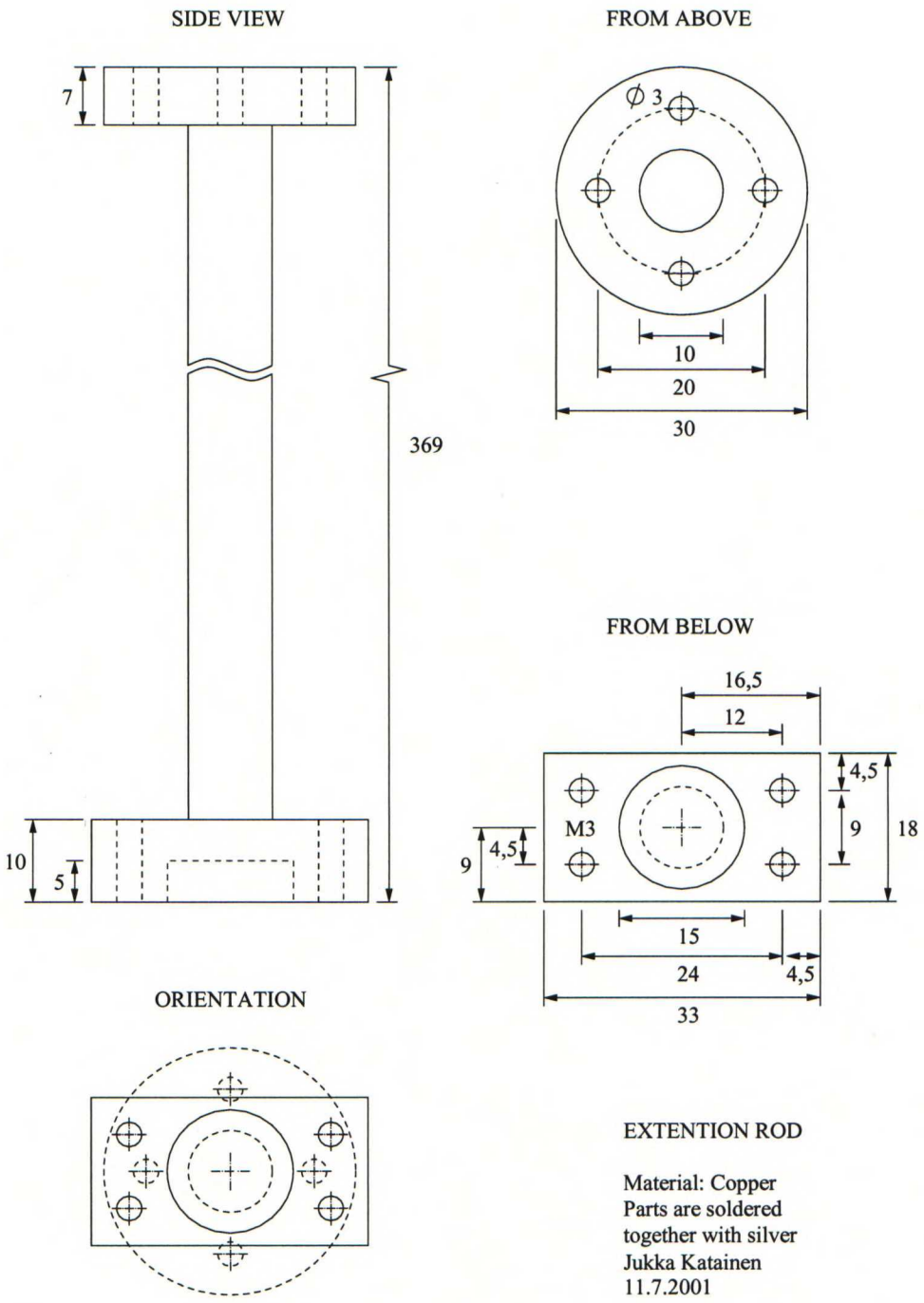


Figure A.13. *Extension rod.*

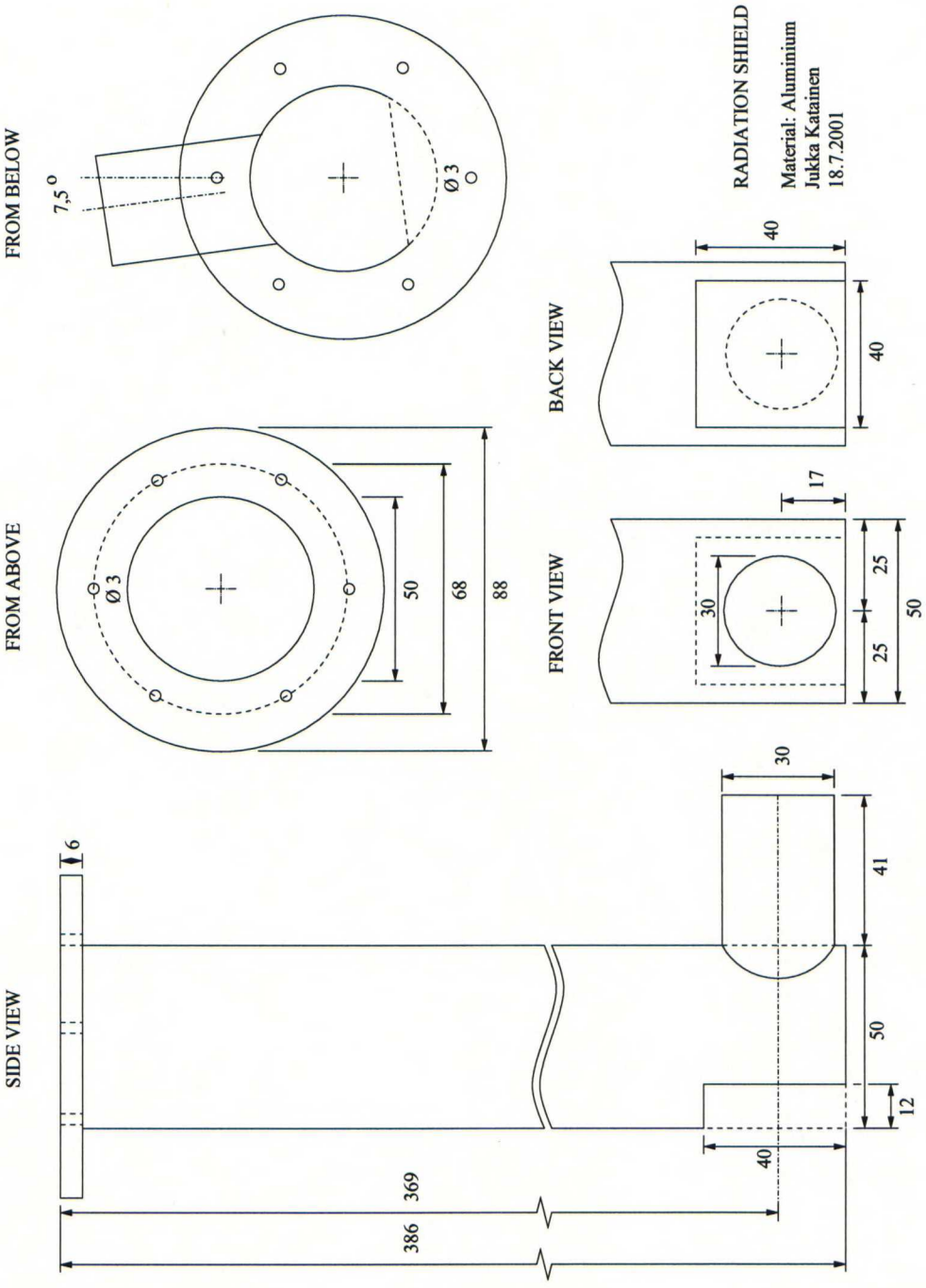


Figure A.14. *Radiation shield.*

# Appendix B

# Measured IV-curves

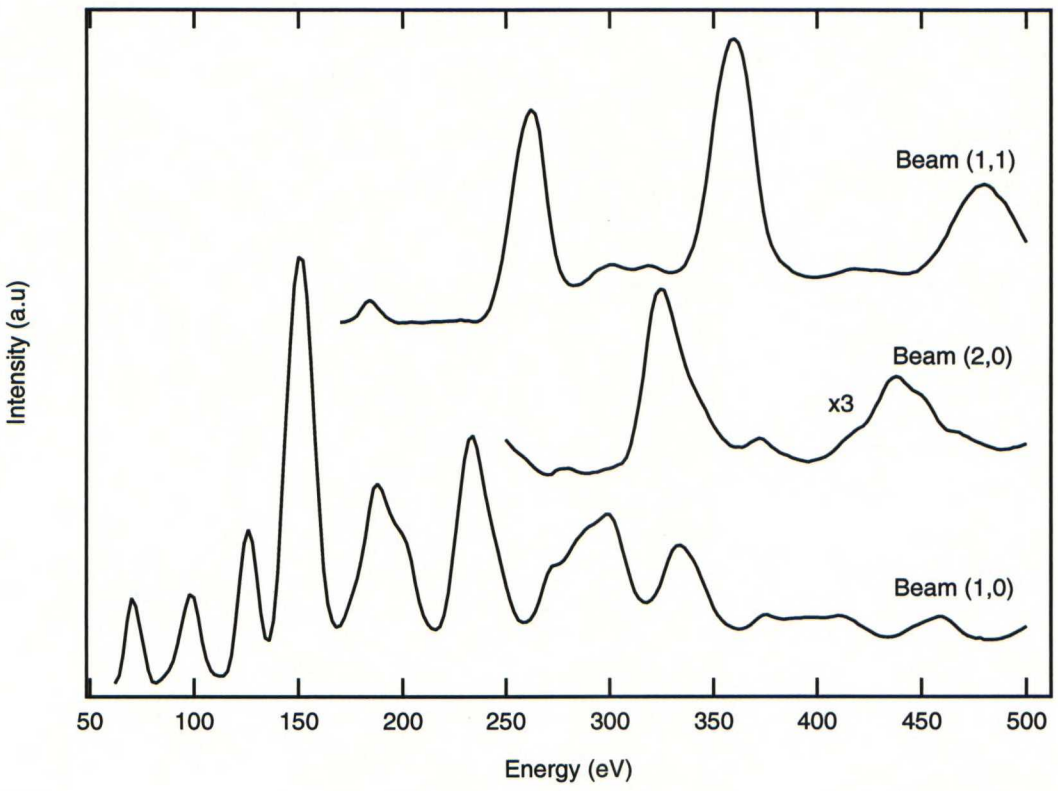


Figure B.1. *Integral order IV-curves from the* $p(\sqrt{7} \times \sqrt{7})R19.1°$ *structure.*

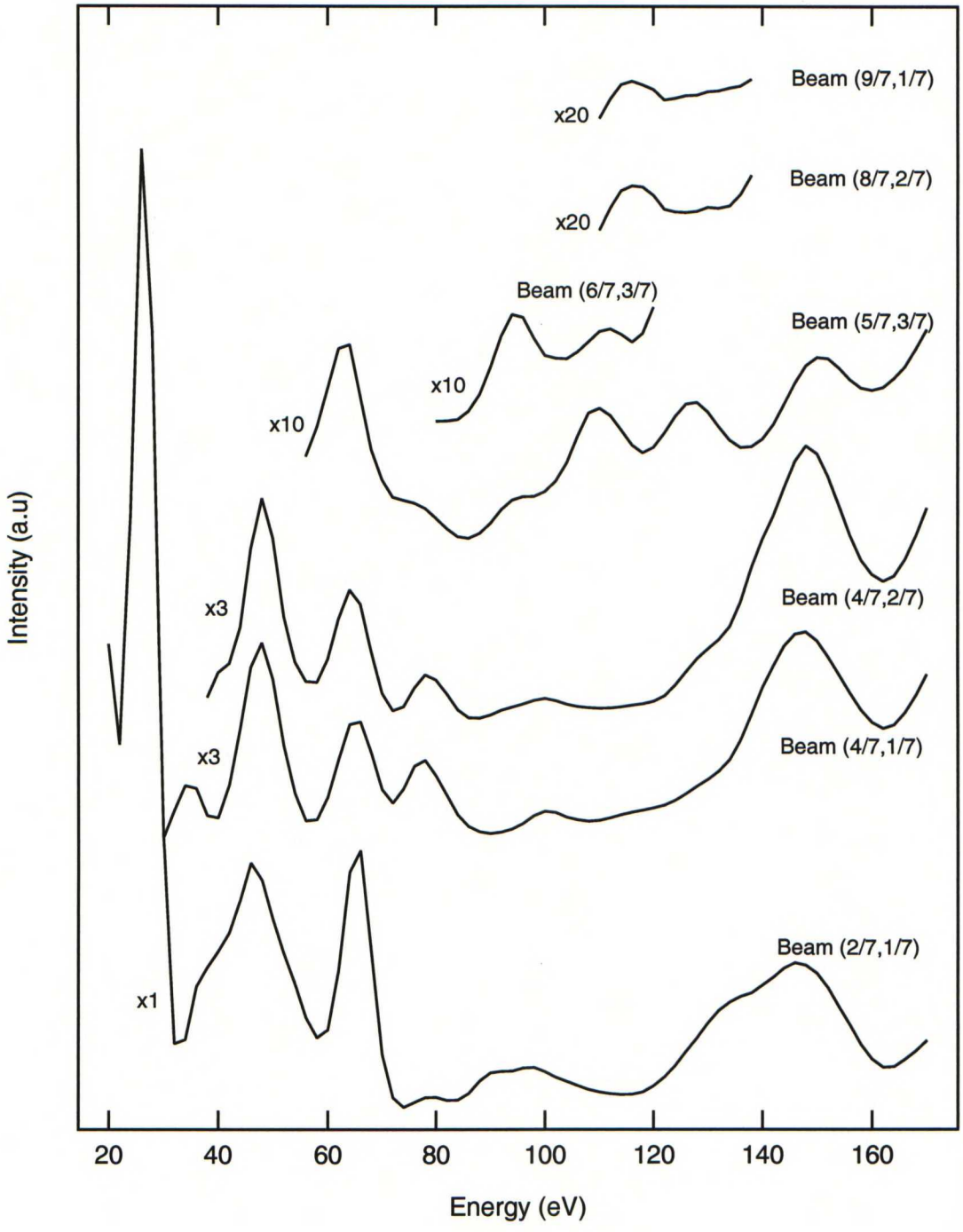


Figure B.2. *Fractional order IV-curves from the* $p(\sqrt{7} \times \sqrt{7})R19.1°$ *structure.*